The Chandra M101 Megasecond: Diffuse Emission
December 14, 2009

K. D. KUNTZ[1]
The Henry A. Rowland Department of Physics and Astronomy, Johns Hopkins University, 3400 North Charles Street, Baltimore MD, 21250
kuntz@pha.jhu.edu

S. L. Snowden[2]
Laboratory for High Energy Astrophysics, Code 662, NASA/GSFC, Greenbelt, MD 20771
snowden@milkyway.gsfc.nasa.gov

ABSTRACT

Because M101 is nearly face-on, it provides an excellent laboratory in which to study the distribution of X-ray emitting gas in a typical late-type spiral galaxy. We obtained a *Chandra* observation with a cumulative exposure of roughly 1 Ms to study the diffuse X-ray emission in M101. The bulk of the X-ray emission is correlated with the star formation traced by the FUV emission. The global FUV/X-ray correlation is non-linear (the X-ray surface brightness is roughly proportional to the square root of the FUV surface brightness) and the small-scale correlation is poor, probably due to the delay between the FUV emission and the X-ray production in star-forming regions. The X-ray emission contains only minor contributions from unresolved stars ($\lesssim 3\%$), unresolved X-ray point sources ($\lesssim 4\%$), and individual supernova remnants ($\sim 3\%$). The global spectrum of the diffuse emission can be reasonably well fitted with a three component thermal model, but the fitted temperatures are not unique; many distributions of emission measure can produce the same temperatures when observed with the current CCD energy resolution. The spectrum of the diffuse emission depends on the environment; regions with higher X-ray surface brightnesses have relatively stronger hard components, but there is no significant evidence that the temperatures of the emitting components increase with surface brightness.

Subject headings: galaxies: X-rays — galaxies: ISM — galaxies: individual (M101, NGC 5457)

1. Introduction

M101 is an excellent target for X-ray studies of the hot ISM. At a distance of only 6.8 Mpc (Saha et al. 2006) the plate scale is 32.5 pc arcsec^{-1}, so the effective resolution is limited by the count rate rather than by the PSF. Although close and large (D_{25}=28.′84, de Vaucouleurs et al. 1991), the bulk of the bright X-ray emitting disk fits within the FOV of a single ACIS chip. Since M101 is close to face-on (i= 27° Kamphuis 1993) correlation of X-ray emission with the underlying disk features is trivial, though separation of disk emission from halo emission is very difficult. Even for its position at $(\ell, b) = (102.0°, 59.8°)$, the absorbing Galactic column is very low, 9×10^{19} cm^{-2}, meaning that X-ray studies of M101 can extend to much lower energies than X-ray studies of other nearby galaxies. As a result of these sterling qualities, M101 has been the object of a great deal of study so that this X-ray study is supported by a plethora of ancillary data, including some gas-phase abundances.

M101 is a prototypical ScI galaxy (Sandage & Bedke 1994) although some classifications place it somewhat later (SAB(rs)cdI, de Vaucouleurs et al. 1991). M101 shows bright nuclear emission in the central 0.′25-0.′5 at most wavelengths. The optical disk inside $\sim 3'$ is relatively uniform with two or three discontinuous arms. Outside of that radius the optical emission is dominated by a series of individual arms that are often strongly bent. The outer disk is strongly asymmetric in H I and the UV. extending much further to the northeast than the southwest. That asymmetry suggests dynamical interaction of M101 with the nearby dwarf galaxy NGC 5471, while the linear arms with angular breaks suggest "massive disturbers" within the M101 disk (Waller et al. 1997). These dynamical interactions may be increasing the star-formation, which is somewhat stronger on the side of the galaxy that is more disturbed. However, although M101 is a vigor-

ously star-forming galaxy, it is by no means a "starburst" galaxy. The specific far-IR flux of M101 is not much greater than that of the Milky Way (provide values here). It should also be noted that M101 has a normal UV morphology and does not have an extended UV disk in the manner of M83 (Thilker et al. 2007).

A number of large star-forming regions in M101 have their own NGC numbers. Of these, NGC 5471, NGC 5462, NGC 5461, NGC 5455, and NGC 5450/NGC 5447 are X-ray bright. Although not all of these objects deserve the label "giant H II regions", for convenience they will be referred to in that manner in this work. The detailed analysis of these objects will not be included here, though some are included in the general analysis of the diffuse emission.

Our previous *Chandra* study of M101 (KSPM, Kuntz et al. 2003) showed that 1) the X-ray emission is correlated with star-forming regions 2) the X-ray emission is well characterized by two thermal components, and 3) the relative contributions of those two components does not vary strongly with location within the disk. Although we argued for a degree of uniformity, the data required averaging over very large areas in order to accumulate enough counts to produce reasonable statistics for the hardness ratio. The object of the current study was to acquire a sufficiently deep exposure that one could measure the hardness ratios over much smaller areas. Measuring the spectral variation with location can then be used to constrain the nature of the underlying emission sources in the absence of the ability to resolve the individual emission sources.

In this study of M101 we will show the following: 1) The global correlation between X-ray and FUV emission is non-linear, and the one-to-one correlation between X-ray and FUV "knots" is poor, as simple considerations of the evolution of star-forming regions would suggest. The correlation can be used to show that the bulk of the X-ray emission is due to current or recent star formation. 2) The global spectrum is not well fit by two thermal components; three thermal components are better, but still unsatisfactory, and simple distributions of emission measure do no better. 3) The spectrum depends upon the local environment; regions with higher surface brightnesses have harder spectra, but there is no strong evidence for higher temperatures, just higher emission measures for the harder components.

In the following paper, §2 describes the data and their initial reduction. We describe the construction and removal of the different backgrounds and foregrounds from the images, and the mosaicking of the X-ray images in §3. A brief comparison of the X-ray, FUV, and optical morphology occupies §§3.2 and 3.3, while §3.4 describes the construction and implications of the hardness ratio maps. We describe the construction of the spectra of all of the components not due to diffuse emission in M101, as well as the external constraints on the spectral fitting in §§4.0 through 4.4. The spectral fits of the global spectrum are described in §4.5, while the change in spectral shape with surface brightness is explored in §4.6. The discussion, §5, is primarily concerned with the fraction of the X-ray emission that is truly diffuse and its relation to the FUV emission. We then compare the results of the spectral fits with those from other spiral galaxies.

In the interest of cleaner typesetting, easier reading, and the conservation of ink, all surface brightnesses in this paper are in units of photons cm^{-2} s^{-1} $arcsec^{-2}$ which will be referred to as surface brightness units (akin to line units) and abbreviated as sbu.

2. Data

2.1. Chandra

The *Chandra* observations were originally planned as six observations with the center of the ACIS-S3 chip placed on the center of the galaxy. The exposures were to be taken two months apart, allowing the natural roll of the spacecraft to place the other ACIS chips in circles covering a large fraction of the outer disk and nearby background. A seventh observation was planned for which the ACIS-S optical axis was placed between the

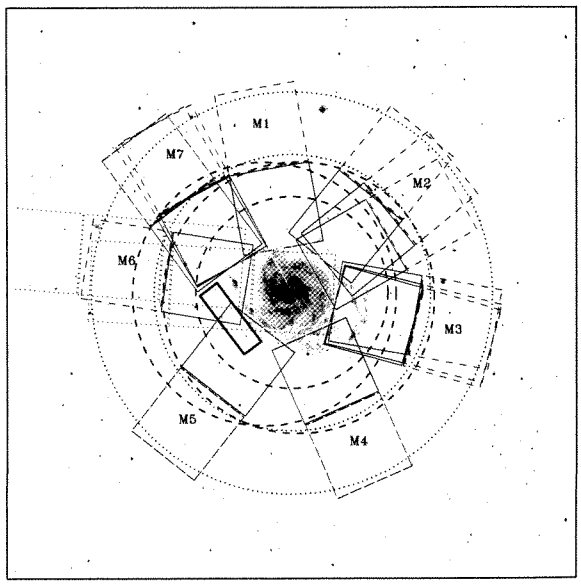

Fig. 1.— The FOV of the various detectors superimposed upon the Digital Sky Survey B2 image. *White squares:* the ACIS-S3 chip positions, *black squares:* the ACIS-S2 chip positions, *dashed black squares:* the ACIS-S1 chip positions, *dotted black squares:* other Chandra data, *dashed black circles:* the *XMM-Newton* FOV (the center is excluded) *inner dotted black circle:* the D_{25} region, *outer dotted black circle:* the inner radius of the annulus from which the *ROSAT* data were extracted.

TABLE 1
M101 EXPOSURES

Exposure Segment	Obsid	Date	PI	Exposure (ks)	Roll (°)	Position (α, δ)	Comments
	934	2000-03-26	Snowden	96.74	150.42	210.8015,54.36679	
	2065	2000-10-29	Prestwich	9.63	3.2	210.8675,54.34844	
	2779	2002-10-31	Wang	11.95	4.9	211.1378,54.39713	
Mega1	4731	2004-01-19	Kuntz	56.24	79.7	210.8207,54.39339	
Mega1	5297	2004-01-24	Kuntz	12.48	79.7	210.8207,54.39339	Residual SPC[a] in S1 and S3
Mega1	5296	2004-01-21	Kuntz	3.22	79.7	210.8207,54.39339	Strong Flares
	5300	2004-03-07	Kuntz	52.09	129.04	210.8037,54.34877	
Mega2	5309	2004-03-14	Kuntz	71.68	141.20	210.7446,54.37879	
Mega2	4732	2004-03-19	Kuntz	70.69	141.20	210.7446,54.37880	
Mega3	5322	2004-05-03	Kuntz	64.70	190.31	210.7261,54.34239	
Mega3	4733	2004-05-07	Kuntz	6.26	194.29	210.7270,54.33924	Strong flares, orig. 24.24ks
Mega3	5323	2004-05-09	Kuntz	42.41	195.71	210.7275,54.33816	
Mega4	5337	2004-07-05	Kuntz	9.94	246.18	210.7693,54.30774	
Mega4	5338	2004-07-06	Kuntz	28.57	246.18	210.7693,54.30774	
Mega4	5339	2004-07-07	Kuntz	14.32	246.18	210.7693,54.30774	Residual SPC in S1 and S3
Mega4	5340	2004-07-08	Kuntz	54.42	246.18	210.7693,54.30774	
Mega4	4734	2004-07-11	Kuntz	35.47	246.18	210.7693,54.30774	
Mega5	6114	2004-09-05	Kuntz	42.17	308.12	210.8497,54.31175	Strong flares, orig. 66.20ks
Mega5	6115	2004-09-08	Kuntz	35.74	308.12	210.8497,54.31174	
Mega5	6118	2004-09-11	Kuntz	11.46	308.12	210.8497,54.31180	Residual SPC in S1 and S3
Mega5	4735	2004-09-12	Kuntz	28.78	308.12	210.8497,54.31175	
Mega6	4736	2004-11-01	Kuntz	70.34	9.29	210.8816,54.35441	
Mega6	6152	2004-11-07	Kuntz	16.31	9.29	210.8816,54.35441	Strong flares, originally 44.09ks Residual SPC in S3 but not S1
Mega7	6170	2004-12-22	Kuntz	47.94	53.702	210.9572,54.36362	Possible residual SPC in S1
Mega7	6175	2004-12-24	Kuntz	40.66	53.702	210.9572,54.36362	
Mega7	6169	2004-12-30	Kuntz	29.37	59.66	210.9568,54.36399	
Mega7	4737	2005-01-01	Kuntz	21.85	61.926	210.9566,54.36415	

[a]Soft Proton Contamination

giant H II regions NGC 5461 and NGC 5462, allowing some fraction of the ACIS-S3 chip to measure the background off of the galactic disk. However, heating of the EPHIN became a problem, so each observation was broken into several (two to five) shorter observations, and the roll angles were allowed to vary. As a point of nomenclature, each of the originally planned observations will be referred to here as an *observation segment*, numbered M1 through M7, each of which is composed of a number of individual *obsids*. To the current program data were added a number of archival exposures All of the data were downloaded from the archive and reprocessed using CIAO 3.4 and CALDB 3.4.

Light Curve Cleaning: For each obsid, the 2.0-7.0 keV light curve was constructed for the ACIS-S3 data, which are most sensitive to soft proton contamination and enhancements in the particle background. We used a method similar to that described in Kuntz & Snowden (2008) to remove time periods strongly affected by soft proton flares. As with all such methods, any relatively constant and/or low intensity soft proton contamination will not be removed.

Point Source Detection/Removal: Point source detection was done with the CIAO routine *wavdetect*. The detections were made in multiple overlapping broad bands, and positions were refined using the cross-correlation of PSF models with the data. The details of the point source analysis will appear elsewhere. Only sources with signal-to-noise ratios greater than three in the 0.5-2.0 keV band were retained in the catalogue used here for point source removal. The point source detection limit was a relatively uniform $L_{0.5-2.0} \sim 10^{36}$ ergs/s over the area covered by the ACIS-S3 chip. Given that the PSF for a single source can be very different from one obsid to the next, the point source removal was done on an obsid-by-obsid basis. The area removed for each point source was elliptical; the eccentricity and the position angle of the ellipse matched the PSF at the source location and the axes were 1.5 times the length of the axes of the 85% encircled energy region. Ultraluminous X-ray sources in their high state, due to the strong wings of the PSF, were given considerably larger exclusion regions, 15″ in radius.

With the exception of supernova remnants (SNR), most point and point-like sources will have non-thermal spectra, so the contribution of residual point sources in the diffuse emission can be isolated spectroscopically. The ChASeM33 survey of SNR (Long et al. 2009) in M33, a low-mass late-type spiral that is an order of magnitude closer than M101, shows that the X-ray luminous SNR typically have diameters smaller than ~ 50 pc, which at the distance of M101 is 1.″4 or ~ 3 ACIS pixels. Thus, individual bright SNR will be detected as point sources and removed; the bulk of the SNR contribution to the diffuse emission will be due to faint

and/or large remnants that are well on their way to losing their identities as separate entities.

Many sources easily seen in the smoothed ACIS-S1 images were not included in the source catalogue generated with *wavdetect* from the ACIS-S1 data. Thus the source catalogue for cleaning the ACIS-S1 data was assembled piecemeal from *wavdetect* and visual inspection of the data smoothed on various scales. The sources were correlated with the *GALEX* FUV emission to ensure that extended emission from M101 was not discarded. As will be seen, this irregularity is not an issue of concern.

Backgrounds and Foregrounds: Both the imaging and spectral analysis require the removal of multiple emission components not related to M101. The fore/background components contaminating the image/spectrum of M101 are 1.) Galactic foreground emission, 2.) extragalactic background emission due to unresolved AGN, 3.) the instrumental particle background, and 4.) the instrumental background due to soft proton flares. Because M101 fills the FOV for the ACIS-S2 and ACIS-S3 chips, there is no single "local fore/background" spectrum to be used to remove all of the components not due to M101. We have used a "first-principles approach" (Snowden & Kuntz 2008) characterizing each of the fore/background components individually, removing them, or fitting them simultaneously with the M101 spectrum. Consequently, there is a significant interplay between the spectroscopic and imaging analyses. As a result of this interplay, discussion of either imaging or spectroscopic analysis in isolation is difficult. We have chosen to discuss the imaging analysis first in §3, with the neccessary discussion of the spectroscopic analysis that was required for the imaging analysis delayed to §4.

2.2. XMM-Newton

XMM-Newton has obtained three observations of M101 to date which are listed in Table 2.

The soft proton flares were removed from each observation using the method described in Kuntz & Snowden (2008). Each of the observations is strongly flared and many time intervals are unusable due to strong soft proton flares. Although the intervals between the flares appear rather quiescent, comparison of the 8.0-12.0 keV count rate in a $11.5' < R < 14.0'$ annulus at the outer edge of the FOV with the same energy interval for the unexposed pixels reveals that there is significant soft proton contamination after the light-curve cleaning. (See De Luca & Molendi (2004) and Kuntz & Snowden (2008) for a complete description of this method.) After light-curve cleaning, $\sim$ 60 ks of data remain.

Point sources were detected in the 0.3-2.0 keV and 2.0-10.0 keV bands using the SAS task *edetect-chain*. For the imaging analysis, point sources having a maximum likelihood estimate of 40 or greater were removed; this criterion is roughly equivalent to a point source detection limit of 1.3×10^{-14} ergs cm^{-2} s^{-1} for these exposures. The point source exclusion regions were circular and contained 85% of the encircled energy, typically 25″ to 28″. Given previous spectroscopic analyses of these data by Warwick et al. (2007), our spectroscopic analysis of the *XMM-Newton* data was more narrowly focused to support the *Chandra* data; it is discussed in §4.5. We have used the data from the EPIC MOS1 and MOS2 detectors; we have not used the data from the PN detector as there is not yet a robust background model for that detector. The particle backgrounds were created using the method of Snowden & Kuntz (2008) for imaging and Kuntz & Snowden (2008) for spectroscopy.

2.3. ROSAT

The *ROSAT* data consist of a single PSPC observation (rp600108) taken 8 June 1991 with the PSPC-B in high gain mode and lasting 32.83 ks. Although multiple HRI images exist, these were not used as they do not contain spectral information. The data were reduced using the *ROSAT* ESAS software (Snowden & Kuntz 1998) to characterize and remove the particle background, the scattered solar X-rays, and the long-term enhancements. We constructed images in the seven standard *ROSAT* bands and then detected and removed background point sources using the same criteria as Snowden & Pietsch (1995). We then constructed radial profiles, and determined the background levels from an annulus with $25' < R < 50'$. The backgrounds were then subtracted. Since the background includes the extragalactic background, which will be more heavily absorbed in the direction of M101 than it will be in the "background" region, it will be oversubtracted. We corrected the M101 flux by adding back to each energy the amount of the extragalactic background absorbed by M101, assuming a Moretti et al. (2003) luminosity function, an intrinsic spectrum with $\Gamma = 1.46$ (Chen et al. 1997), and a normalization of 9.5 keV/cm^2/s/sr/keV (Kuntz et al. 2001).

2.4. GALEX

The *GALEX* images of M101 were downloaded from the MAST archive. Since the pipeline background subtraction is inappropriate for the analysis of diffuse emission, we used the flat-fielded image (the "int" files) and determined the background from regions far from the galaxy from which the point sources had been manually excluded. The background levels removed were 5.5×10^{-4} and 2.1×10^{-4} sbu for the NUV and FUV filters respectively. By comparing the *GALEX* images, *XMM-Newton* OM images, and HST images, we were able to identify the UV bright foreground stars and remove them from further analysis.

TABLE 2
XMM-NEWTON M101 EXPOSURES

Obsid	Date	PI	Filter	Total Exposure (ks)	Useful[a] Exposure (ks)	Position (α, δ) (J2000)	Comments
0104260101	2002-06-04	Watson	Medium	42.73	21.88	210.7917,54.34000	some SPC[b]
0164560701	2004-07-23	TOO-Kong	Medium	32.83	21.78	210.8846,54.35083	strong SPC and SWCX[c]
0212480201	2005-01-08	TOO-Kuntz	Thin1	32.08	16.23	210.8862,54.35056	strong SPC

[a]Amount of time left after light-curve cleaning.

[b]Soft Proton Contamination

[c]Solar Wind Charge Exchange contamination

As can be seen in Figure 2, the extinction in the FUV band is stronger than even the softest part of the Chandra bands. We therefore extinction corrected the FUV data using the A(FUV) as a function of radius relation for M101 shown in Figure 9 of Boissier et al. (2007).

3. Imaging Analysis

3.1. Mosaicking

The image of M101 shown in Figure 3 was produced by mosaicking all of the obsids from the current observing program. Obsid 2779 was too offset and too short to add significant data. Obsids 934 and 2065 were both taken in AO-1, when the response and blocking filter absorption was very different from the current observations (see §4.5) As a result, we have not included them in the mosaic.

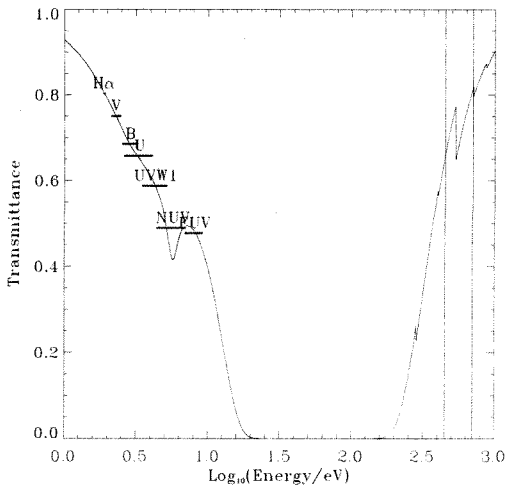

Fig. 2.— The relative transmission of the Galactic ISM as a function of energy assuming Galactic dust and E_{B-V}=0.1, equivalent to N_H=4.7×10^{20} cm^2.

For each chip of each obsid we created count images at the full resolution of the detector for each energy band of interest, the corresponding exposure map, and a point source mask. For each chip of each obsid, the mask was applied to each of the energy band images. The image, the exposure map, and the mask were then rebinned into a standard coordinate system. To produce the final mosaic in a given energy, the individual count images were summed, a particle background image, a Galactic foreground emission image, and an extragalactic background emission image were subtracted. The result was then divided by an effective exposure map appropriate for the spectral shape of the bulk of the M101 emission. The relative number of counts in each component is given in Table 3.

The Particle Background Image: The response of the instrument to the particle background is determined from data taken while the instrument is in the stowed position[1], out of the focal plane and under a shield. It is thought that the particle background experienced by the ACIS instrument in its stowed position is very similar to the particle background that it experiences when in the focal plane. The response to the particle background is not flat, and its structure varies with energy. It is assumed that although the intensity of the particle background changes with time, the shape of the response to the particle background does not. To determine the distribution of particle background counts, the events from the appropriate energy band in the stowed event list were cast into chip images, events falling on inactive pixels were removed, and the resulting image binned by 32 and smoothed. This procedure retains the large-scale structure of the particle background while reducing the small-scale structure that may be due to statistical variation. This image was then rebinned to the full resolution, inactive pixels were removed, and the image normalized to unity. This image was then used as an instrument map for the creation of an exposure map, which could then be multipled by the total number particle background counts. The total num-

[1]http://cxc.harvard.edu/contrib/maxim/stowed/

TABLE 3
COMPONENT COUNTS

Component	ACIS-S3		ACIS-S2		ACIS-S1	
	0.45-0.7 keV (counts)	0.7-1.0 keV (counts)	0.45-0.7 keV (counts)	0.7-1.0 keV (counts)	0.45-0.7 keV (counts)	0.7-1.0 keV (counts)
Point Sources[a]	14853.0	18694.0	3229.0	9117.0	4348.0	5720.0
Point Sources[b]	11937.2	16631.7	1297.0	4225.0	...	...
Raw (excluding point sources)	56214.0	46123.0	9296.0	10727.0	25370.0	22454.0
Particle Background	17080.0	17098.2	5647.2	6241.9	17712.6	17981.9
Galactic Foreground	7936.6	2516.9	2430.8	1369.5	6063.8	1884.9
Extragalactic Background	996.9	2093.3	435.2	1386.2	1421.5	2163.7
Remainder (M101)	30200.5	24414.6	782.8	1729.4	162.0	417.5
Soft Proton[c]	210.0	250.0	...	...	240.0	255.0

[a] Number of counts in regions rejected for containing point sources. Of these counts, the regions excluded for the transient ultraluminous sources account for 4425 and 4303 counts in the .45-0.7 keV and 0.7-1.0 keV bands.

[b] Number of counts in point sources after local background subtraction. Of these, the transient ultraluminous sources account for 3620.2 and 3685.6 counts in the .45-0.7 keV and 0.7-1.0 keV bands. These values were not calculated for sources on the ACIS-S1 chip.

[c] Estimate of contribution from spectroscopic fitting. The soft proton contamination was not removed from the images.

ber of background counts in a particular energy band was determined from the spectrum of the stowed data normalized by the observed number of counts in 10.5 keV < E < 12.4 keV where the instrument response to X-rays is negligible.

The Galactic Foreground Image: Since the spectral shape of the Galactic foreground is significantly softer than the M101 spectrum (due to the unabsorbed Local Hot Bubble/Solar Wind Charge Exchange component) and the response changes rapidly at the energies of interest, we used the model of the Galactic foreground spectrum (§4.2) to create an effective area map for the Galactic foreground, and from that created an image of the raw counts due to the Galactic foreground.

The Extragalactic Background Image: We produced the extragalactic background image in a similar manner. The spectral shape of the extragalactic background was taken to be a powerlaw with a photon index of 1.46 (Chen et al. 1997). The normalization was taken from the spectral fitting (§4.2). Since the extragalactic background is absorbed by the neutral and molecular gas in M101, the extragalactic background map was corrected for that absorption using the H I map of Kamphuis (1993) and the ^{12}CO map of Helfer et al. (2003). Clearly the spectral shape of the background changes with absorption, and thus the appropriate effective area map changes with location. To correctly compensate is a computationally intensive task. Noting that the effective exposure maps are least flat at the chip edges and that our observing strategy for the S3 chip places the chip edge where the absorption will be the lowest, the M101 signal the lowest, and the background signal the highest, we chose to calculate the effective area maps for the more lightly absorbed regions, where the wrong response would produce the biggest error.

The Soft Proton Contamination The spatial distribution of the soft proton contamination is not well characterized for the ACIS instrument (Appendix A). Since, for all obsids used in this analysis, the soft proton contamination was small, 5.8×10^{-10} (6.9×10^{-10}) sbu in the 0.45-0.7 keV (0.7-1.0 keV) band, no attempt was made to remove it from the images.

3.2. The Image

The spectrum of M101 discussed in §4.5 can be seen to have little emission at $E > 1.0$ keV. Below 0.45 keV, the backgrounds and the corrections for the blocking filter absorption become increasingly uncertain. Thus, we have restricted imaging analysis to $0.45 < E < 1.0$ keV, the band shown in Figure 3. We have not included the data from the ACIS-S1 chip in this mosaic as they do not include emission due to M101. Because the ACIS-S2 chip has significantly poorer soft response than the ACIS-S3 chip, only the brightest X-ray emitting regions (generally giant H II regions) are clearly visible in the image, although the general decline of the disk emission with radius can also be seen.

There are a number of knots of emission surrounding excised point sources. In each case we have examined the original images carefully to determine that the emission is truly diffuse and not the relict wings from bright sources. Given that HMXB and young (small) SNR should preferentially be found in star-forming regions, where there is likely to be X-ray emission due to winds or more diffuse supernovae, then one might be surprised if the most intense X-ray knots did *not* have embedded point sources.

Comparison of the X-ray image with the HST image shows that at the level of 2.6×10^{-9} sbu most of the X-ray knots are identifiable with either individual H II regions or larger star-forming complexes. Only a few knots can be identified with foreground stars just

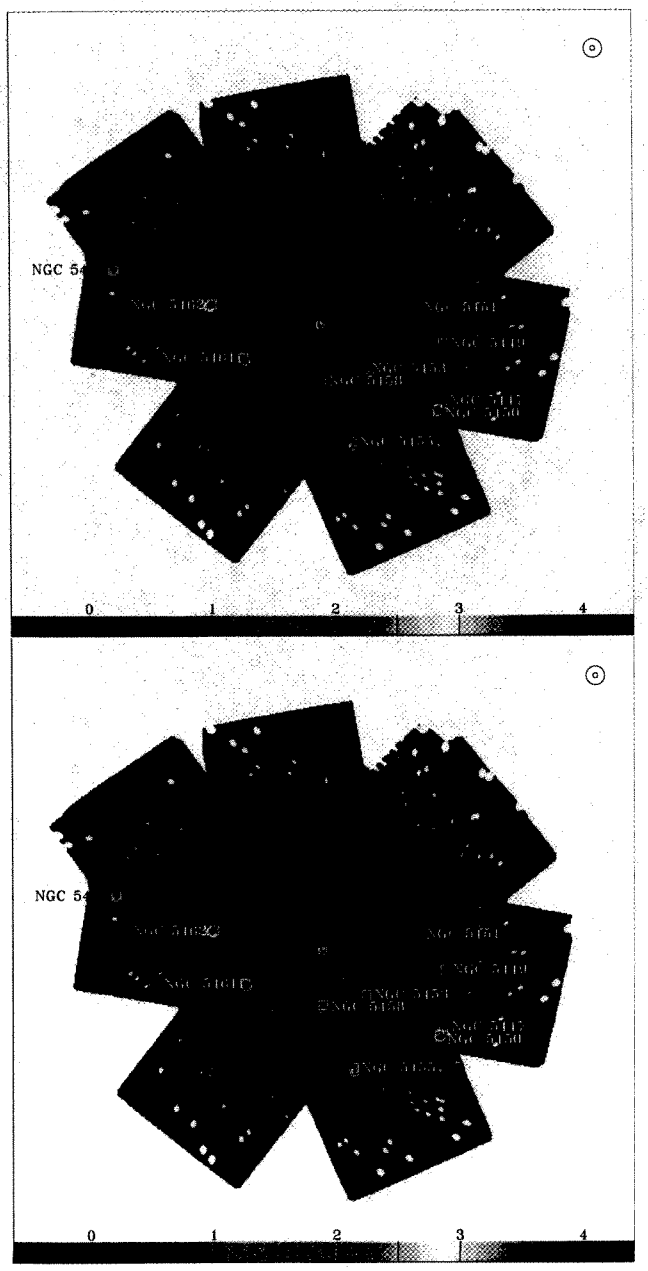

Fig. 3.— **Top:** A mosaic in the 0.45-1.0 keV band of the data obtained from the ACIS-S3 and ACIS-S2 chips after point source removal, the removal of the foregrounds and backgrounds, and correction by the effective area map. The image was smoothed by a Gaussian with $\sigma = 7\farcs87$ (16 native pixels), the smaller circle in the upper right. The large circle in the upper right has a diameter of $1'$. The labels on the key are in units of 10^9 sbu. White regions have no data or have been excluded. The black contours mark the overlap of the ACIS-S3 and ACIS-S2 fields. The giant H II regions in the NGC catalogue are also marked. **Bottom:** A mosaic in the 0.45-1.0 keV band of the data obtained from only the ACIS-S3 chip. The image was smoothed by a Gaussian with $\sigma = 3\farcs94$ (8 native pixels), the smaller circle in the upper right. The white contours mark a surface brightness of 2.6×10^{-9} sbu in the image smoothed by a Gaussian with $\sigma = 3\farcs94$. The black contours mark a surface brightness of 4.1×10^{-10} sbu in the image smoothed by a Gaussian with $\sigma = 7\farcs87$.

below the X-ray point source detection threshold (2) or clusters of galaxies (1). Several more stars and a background galaxy are associated with knots at 1.3×10^{-9} sbu.

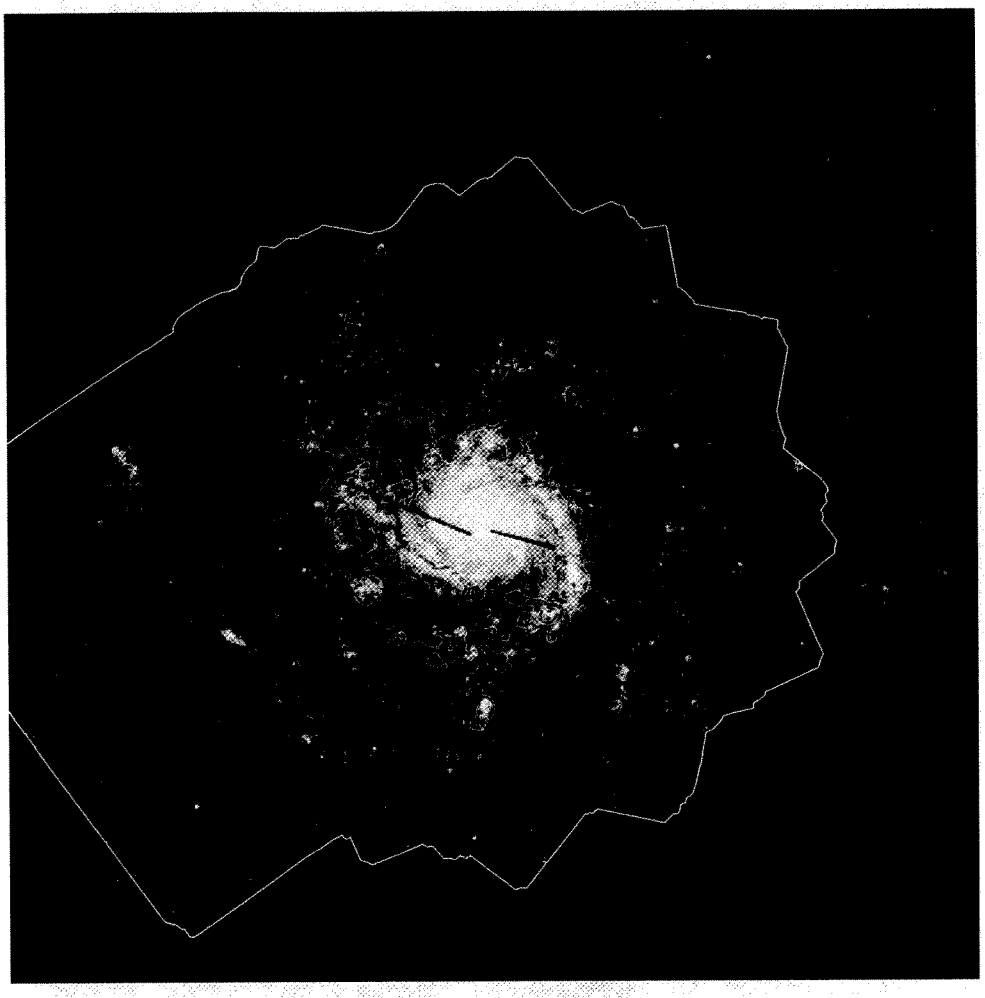

Fig. 4.— A mosaic of *HST* ACS images of M101. The f435 image has been assigned to blue, the f555 image to green, and the f814 image to red, so that H II regions appear green, massive stars appear blue, and late-type stars and background galaxies appear yellow to red. The contours are the ACIS-S3 X-ray data smoothed by a $\sigma = 3\farcs94$ Gaussian and are at 1.28×10^{-9}, 2.56×10^{-9}, and 4.13×10^{-9} sbu. The *HST* data were obtained in observing programs by Bresolin (Bresolin 2007) and by Kuntz, astrometrically corrected and mosaicked.

Comparison of the X-ray and *GALEX* FUV images shows a more complex relation between star-formation and the X-ray emitting gas. Within the 1.28×10^{9} sbu X-ray contour there is FUV emission. However, there are many regions of FUV emission of comparable strength without comparable X-ray emission. Although many FUV and X-ray "knots" coincide, there are many FUV knots without corresponding X-ray enhancements and there are a few X-ray knots without obvious FUV enhancements. We also note that the bright east-fainter west asymmetry seen in the FUV is also seen strongly in the X-ray.

3.3. The Radial Profile

The radial profile of the 0.45-1.0 keV emission is shown in Figure 6. The emission due to M101 extends to at least $8'$, or $\sim 0.6 \times D_{25}$. Note that the radial profile calculated from the ACIS-S3 chip does not match the profile calculated from the ACIS-S2 chip because the only region at $R > 5'$ covered by the ACIS-S3 chip is the region around the X-ray bright NGC 5462, while the ACIS-S2 chip covers $R > 5'$ more uniformly. Given the poor soft response of the ACIS-S2 chip and the fact that only the faintest part of the disk falls on it, data from the ACIS-S2 chip are not used in most further analyses. XMM Comparison

3.4. The Hardness Ratio

From the spectra of M101 shown in §4.5 one can see that the primary features of the spectrum are the O VII triplet at 0.56 keV, the O VIII line at 0.65 keV, and the "Fe-L complex" (0.75-1.1 keV) that contains

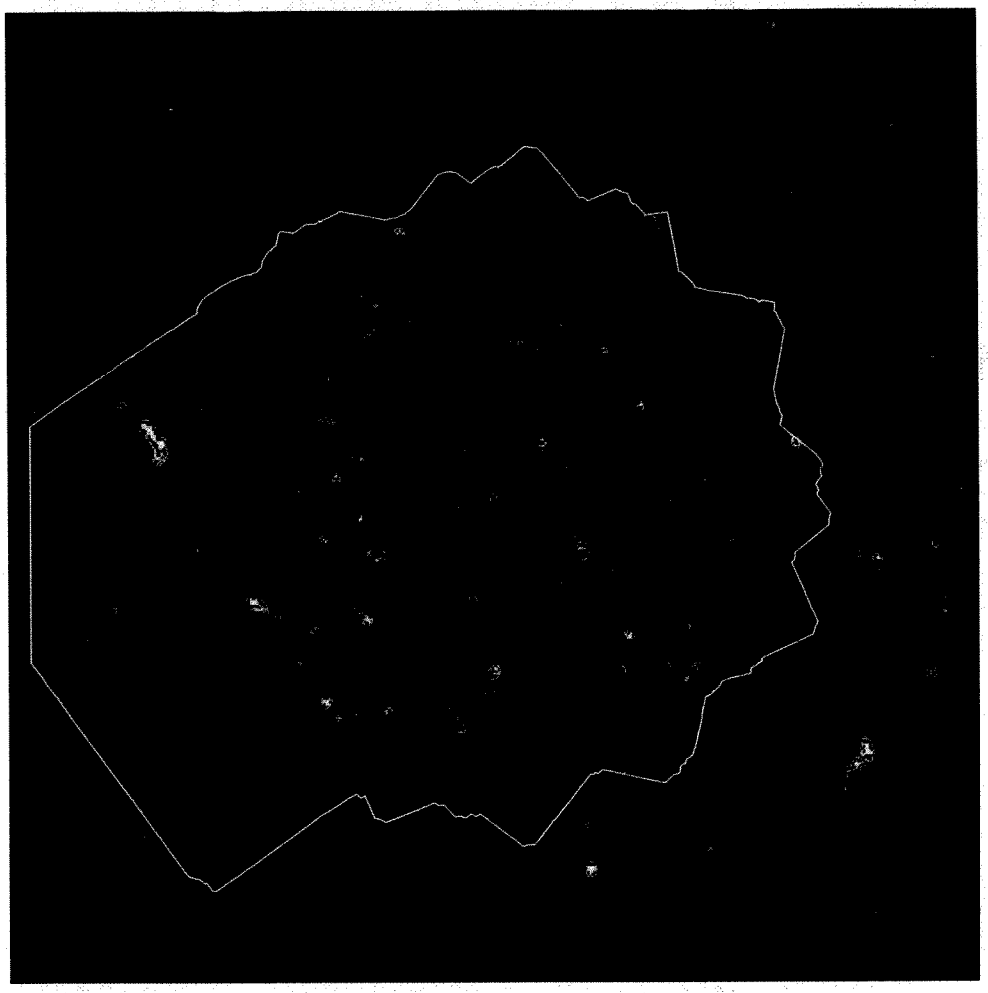

Fig. 5.— The *GALEX* image of M101. The contours are the ACIS-S3 X-ray data smoothed by a $\sigma = 3\farcs94$ Gaussian and are at 1.28×10^{-9}, 2.56×10^{-9}, and 4.13×10^{-9} sbu.

multitudinous unresolved O, Fe, and Ne lines. As in the previous analysis of M101, we created band images that reflect the gross spectral structure, a 0.45-0.7 keV band and a 0.7-1.0 keV band image, and constructed the (0.7-1.0 keV)/(0.45-0.7 keV) hardness ratio. The hardness ratio images are shown in Figure 7. Given the large dynamic range in X-ray surface brightness, hardness maps at a single angular scale can be misleading; we show the hardness ratio maps contructed from band images smoothed with Gaussians with $\sigma = 15\farcs74$, $7\farcs87$, and $3\farcs94$ (32, 16, and 8 ACIS pixels). Regions where the hardness ratio had a S/N< 3 have been removed.

Two regions have clearly higher hardness ratios, the giant H II regions NGC 5461 and NGC 5462. The high region at the extreme right of the most smoothed map is not due to any clearly identifiable feature, though it persists into the next higher resolution map. The most strongly smoothed map suggests that the weaker emission is softer. At higher resolution, only a few small regions appear to have higher hardness ratios, and there is no clear correlation with surface brightness.

Figure 8 shows the hardness ratio as a function of radius and of surface brightness. There is no strong radial gradient in the hardness ratio. If there is either an extended bulge or halo then it must be weak compared to the disk emission or have a hardness ratio similar to the disk. A decrease in 0.05 in the hardness ratio corresponds to a decrease in [Fe/O] of -0.137 so there is no significant gradient in [Fe/O], although M101 has a strong gradient in [O/H] (Bresolin 2007; Kennicutt et al. 2003). Excluding the giant H II regions, the hardness ratio is relatively flat to $\sim 6'$, at which point there is very little signal from M101.

The hardness ratio does seem to be a function of the surface brightness for surface brightnesses greater than $\sim 2.5 \times 10^{-9}$ sbu; below that value the hardness ratio is roughly constant. Very little area has such high surface brightness, and the bulk of that area is due to the giant

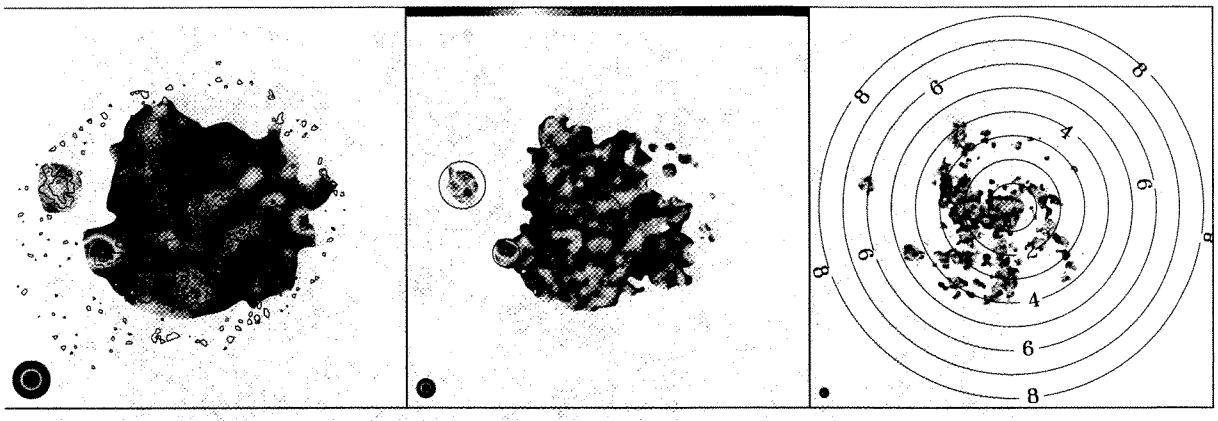

Fig. 7.— The (0.7-1.0 keV)/(0.45-0.7 keV) hardness ratio created by the division of the smoothed hard band image by the smoothed soft band image. The color scale is from 0 to 2.0. The Gaussian smoothing kernels are shown in the lower left of each frame and have σ of 15.″74, 7.″87, and 3.″94 from left to right. **Left:** The image smoothed by a Gaussian with σ = 15.″74. The contours are at the X-ray surface brightness for the image smoothed by a Gaussian with σ = 3.″94 and are at surface brightness levels of 1.3, 13.0, and 41.3 × 10^{-9} sbu. **Middle:** The image smoothed by a Gaussian with σ = 7.″87. The circles show the regions excluded from some analyses as either giant H II regions or the bulge. **Right:** The image smoothed by a Gaussian with σ = 3.″94. The contours mark the distance from the nucleus in arcminutes.

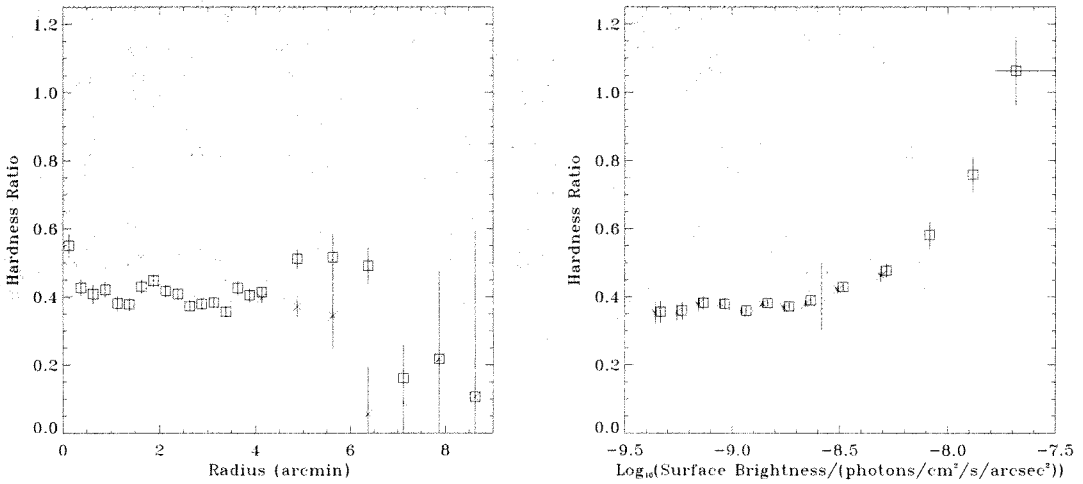

Fig. 8.— **Left:** The hardness ratio as a function of radius. Boxes mark the relation for all parts of the ACIS-S3 mosaic; the × symbols mark the relation after the exclusion of NGC 5461, NGC 5462, and the bulge region. **Right:** The hardness ratio as a function of surface brightness. The symbols are as in the previous panel. The × symbols have been offset in surface brightness for clarity.

H II regions. We defined circular regions surrounding both giant H II regions (and the bulge) that included their emission to below 2.5 × 10^{-9} sbu, excluded those regions, and reconstructed the hardness ratio-surface brightness relation. The relations including and excluding the giant H II regions follow one another; the relation excluding the giant H II regions merely ends at a lower surface brightness. In both cases, the first two points above 2.5 × 10^{-9} sbu have significantly higher hardness ratios than the fainter emission. The relative flatness of the hardness ratio below 2.5 × 10^{-9} sbu should not be interpreted as a lack of spectral change below that value, merely that this choice of bands is insensitive to changes below that surface brightness threshold.

3.5. Summary

The diffuse emission from M101 extends to ∼ 0.6×D_{25}. At larger radii the diffuse emission traces only the brighter star-forming regions. More sensi-

tive images would likely show X-ray emission tracing even fainter arms. The overall correlation of the FUV and the X-ray is good, but the detailed correlation of the FUV knots with X-ray knots is poor. As will be discussed in §5.1, this is to be expected even if all of the X-ray emission were due to star formation. In agreement with KSPM, we find that there is no signficant radial variation in the hardness ratio out to $\sim 6'$. Contrary to KSPM, we find that the hardness ratio increases with surface brightness.

4. Spectroscopic Analysis

As discussed in the imaging section, there are multiple fore/background components to be characterized. The following subsections treat with each of the fore/background components. We then consider each of the outside constraint placed on the spectral fit, before fitting the global spectrum of M101. We then fit the spectra of smaller regions in order to determine the source of the surface brightness-hardness ratio relationship.

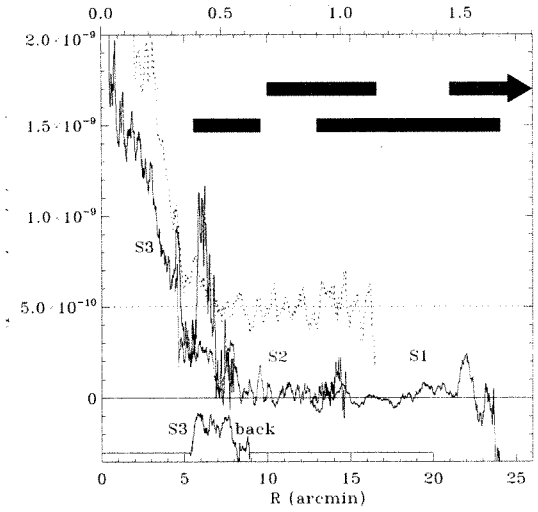

Fig. 6.— The radial profile from the 0.45-1.0 keV band mosaics of the ACIS-S3, ACIS-S2, and ACIS-S1 data after point source removal and fore/background subtraction. The ACIS-S3 data has been smoothed by 1.″5 while the remainder of the data has been smoothed by 17″. The peak in the S3 curve between 5′ and 8′ is due to NGC 5462, and was not included in the ACIS-S3 background region. The radial profile of the ACIS-S3 background region is shown offset downwards by 3×10^{-10} sbu. The radial profile derived from the *XMM-Newton* data is shown by a dotted line offset upwards by 5×10^{-10} sbu. The heavy black bars indicate the radial extent of the background regions derived from various detectors/instruments and missions. See §4.2 for further discussion.

4.1. The particle and soft proton backgrounds

The Particle Background: The particle background spectrum for each chip of each obsid was constructed from the stowed data. We assumed that the intensity of the particle background changes with time, but the shape of the particle background spectrum does not. Hickox & Markevitch (2006) have shown that the band ratios of the particle background spectrum derived from stowed data (typically 40 ks observations) are relatively constant, which is very different from the *XMM-Newton* background (Kuntz & Snowden 2008) and suggests that the particle background experienced by the ACIS instrument is more stable than that experienced by the EPIC instruments.

The particle background spectrum obtained from the stowed data must be normalized to the particle background strength during the observation of interest. Above 11.5 keV the ACIS-S detector has virtually no response, so all counts obtained at higher energies are due to the particle background. We noticed some variability in the shape of the particle background above 13.5 keV. Thus, we take the observed count rate in 11.5 keV <E<13.5 keV as a measure of the particle background rate and normalize the stowed data to that value. Using the count rate in 9.5 keV <E<11.5 keV produces essentially the same results.

Soft Proton Contamination: The light curve cleaning described in §2.1 removes only a part of the soft proton contribution; further measures must be taken to remove or characterize the remainder. Using a unit diagonal response, the spectral shape of the soft proton contamination for the backside-illuminated ACIS chips can be described by

$$N_C \exp\left(\frac{E_c}{E}\right) \quad (1)$$

where the cutoff energy, E_c, ranges from $\sim$ 3 keV to such large values that the spectrum is essentially flat (Markevitch et al. 2003, as well as Appendix A). In the case of a strong flat soft proton spectrum, the spectral region used for normalizing the particle background will be contaminated by the soft proton spectrum and the normalization of the particle background can be significantly overestimated.

The spectrum of the unresolved background is thought to be relatively uniform, and the Milky Way and M101 emission does not extend to energies much above 1.5 keV. Thus, one can check for soft proton contamination in a given obsid by comparing the spectrum for that obsid with the mean spectrum after both have been cleaned of point sources. A significant spectrally smooth residual above 1.5 keV indicates soft proton contamination. Almost all of the spectra extracted from the individual obsids fall in a narrow band surrounding the mean spectrum with a width equivalent to the uncertainty of a typical spectrum. Four spectra

show soft residuals (obsids 6118, 5339, 5297, 6152), and all four are either observations too short to detect low-level flare emission, observations with minor variation in the light curve suggesting low-level flare emission, or observations from which strong flares have been removed. Given the difficulty of determining the correct particle background normalization in the presence of strong soft proton contamination, these obsids were removed from further consideration.

After subtracting the particle background spectrum from spectra extracted from large fractions of the FOV, there is residual emission in the 8-10 keV region. It is not clear whether this residual is due to 1) a slightly incorrect scaling of the stowed spectrum, 2) a slight difference between the stowed spectrum and the particle background spectrum experienced by the instrument when it is in the focal plane, or 3) some other background component. In Appendix A we show that the residual soft proton spectrum for ACIS-S3 becomes quite flat at very low levels, while the spectrum for ACIS-S1 is usually flat. Therefore it is not inconceivable that this residual is due to soft proton contamination. The ACIS-S2 chip is insensitive to soft protons so there should be no such residue in the ACIS-S2 spectrum. However, the energy band one would check (8-10 keV) has a very strong instrumental line in the ACIS-S2 spectrum so the comparison is equivocal. When characterizing the residue as soft proton contamination, the normalization of this component is quite low and tends to affect only the normalization of components extending to high energies such as the extragalactic background.

4.2. The Galactic Foreground & Extragalactic Background

There are three potential sources for the spectrum of the fore/background.

An edge of the ACIS-S3 chip: The aimpoint of the last segment of the *Chandra* observing program was specified to place it between the giant H II regions NGC 5461 and NGC 5462. The FOV was rolled to place about a quarter of the ACIS-S3 chip off of the disk beyond the straight spiral arm that connects the giant H II regions. Spectra were extracted from the X-ray dark region outside the spiral arm, and point sources were excluded as described above (§2.1). The advantage of this measure of the fore/background is that it is on the same detector as the source.

From Figure 3 it can be seen that this region is more X-ray "dark" than that used by KSPM, the area between NGC 5462 and the disk. However, this region is not entirely UV dark, suggesting that even this region may contain a low level of star formation, and thus a low level of X-ray emission due to M101. Indeed, subsequent construction of the radial profile seen in Figure 6 shows that the ACIS-S3 background region contains significant emission from M101.

The ACIS-S1 chip: For all observation segments the ACIS-S1 chip falls outside of the D_{25} region. For most observation segments (not M1 or M6) the ACIS-S1 chip falls beyond the diffuse optical emission associated with extended spiral arms. Thus, one would expect most ACIS-S1 chip spectra to measure the fore/background emission with minimal contamination by M101. However, because the spectra are extracted from a different detector, there are cross-calibration issues, and since the detector is further from the optical axis, the point source removal is problematic.

The regions covered by the ACIS-S1 chip is shown in Figure 1. The point sources were excluded in the same manner as they were for the ACIS-S3 chip, and obsids previously seen to have soft proton contamination were excluded from the analysis. Given the distribution of optical emission associated with the extended spiral arms, one might expect a similar morphology in the 0.4-1.0 keV energy band images obtained with the ACIS-S1 chip, but there is no clear structure in the smoothed X-ray images. However, observations falling on the extended spiral arms were removed from the background region (those obsids marked M1, M6, and M7).

XMM-Newton data: The X-ray radial profile suggests that the X-ray emission drops significantly beyond $R = 8'$, though the arm at $R \sim 10'$ may make a significant contribution. For the *XMM-Newton* background regions we included the area within $13.75'$ of the optical axis but excluded the region with $R < 10'$. As can be seen from Figure 6 this fore/background region extends inside D_{25}, but does not contain significant X-ray emission from M101. As with the ACIS-S1 data, there are detector cross-calibration issues, and given the differences in detectors, optical system, etc., the issues are more significant than with the ACIS-S1 data.

The *XMM-Newton* data are more sensitive to soft proton flares and all of the M101 data sets taken with *XMM-Newton* were strongly flared. Given the relative weakness of the Galactic foreground emission, we have used only the data from obsid 0164560701 as it has the least flare problem.

ROSAT All-Sky Survey Data: In all the above cases, the spectrum extends no lower than $E \sim 0.35$ keV. Since the Galactic emission components are quite soft, the bulk of their emission falls below this energy and so the fit will not be well constrained. We have used the *ROSAT* All-Sky Survey (RASS) spectral energy distribution (SED) from an annulus with $20' < R < 60'$ to constrain the fit to the fore/background. The RASS data are a spectral energy distribution (SED) in six bands (R1-R7) from which the scattered solar X-ray and Long Term Enhancement (LTE) contamination was removed as thoroughly as possible by the *ROSAT* project (Snowden et al. 1997). As a result, the RASS

provides a measure of the diffuse cosmic background far superior than that produced by *ROSAT* pointed observations. The RASS data were extracted using the X-ray background web tool hosted by the HEASARC[2]. The version of the RASS data used is that described by Snowden et al. (1997); the point sources were removed to slightly different levels in the R12 and R47 bands, but the consequent offset in the different bins of the SED is smaller than the uncertainties. We have not used the pointed *ROSAT* data for determining the background as they retain a large unknown residual LTE contamination, while the RASS data have the best possible LTE removal.

Fitting the Fore/Background Spectrum: For the data from each instrument, the Galactic foreground and extragalactic background was fitted with a model of the form

$$A\left[N_L\mathcal{A}(kT_L) + e^{(\sigma N_H)}\left((N_D\mathcal{A}(kT_D) + N_\Gamma E^{-\Gamma})\right)\right]. \quad (2)$$

The APEC model terms $\mathcal{A}(kT_i)$ represent the unabsorbed Local Hot Bubble ($i = L$) emission[3] and the more distant Galactic halo emission ($i = D$) absorbed by the total Galactic column of neutral gas. The $N_\Gamma E^{-\Gamma}$ term represents the unresolved extragalactic background. A is the area over which the spectrum was extracted, so the normalizations are per angular measure. For the ACIS-S1, ACIS-S3, and *XMM-Newton* data, the fit also includes a term for the soft proton contamination. For the *XMM-Newton* data, the fit must also include the Al and Si instrumental lines at 1.49 keV and 1.75 keV which are not removed by the characterization of the particle background (Kuntz & Snowden 2008). The *Chandra* and *XMM-Newton* data are fitted between 0.35 keV and 10.0 keV. Although the Galactic emission does not extend significantly above 2 keV, one must fit to higher energies to properly constrain the unresolved extragalactic background and the soft proton contamination. In each case, the data were fitted simultaneously with the *ROSAT* data.

Since the Galactic foreground varies on degree scales, and since the *ROSAT* data have poor spectral resolution, the normalization of the Galactic foreground in the *ROSAT* data were allowed to differ from that in the *Chandra* or *XMM-Newton* data, but the spectral shape was forced to be the same. The normalizations of the extragalactic background were calculated from the point source exclusion limits, which are very different over these data sets.

The results of the fitting are shown in Table 4. The temperatures of the Local Hot Bubble and the Galactic Halo are consistent among the different data sets though the *XMM-Newton* fit seems to favor lower temperatures. The normalizations of the thermal components for the ACIS-S3 and *ROSAT* data are consistent, the ACIS-S1 and *XMM-Newton* normalizations are significantly (60%) lower. Since the radial profile demonstrates that the ACIS-S3 background region is contaminated by M101 emission, its agreement with the *ROSAT* data suggests that the *ROSAT* annulus is brighter than the ACIS-S1 region. The fitted spectral shapes for the soft proton contamination are consistent with those given then Appendix A (for the ACIS detectors) and Kuntz & Snowden (2008) (for the MOS detectors). Thus we have taken the fit parameters from the ACIS-S1 fit to model the Galactic foreground in the direction of M101.

The normalization of the extragalactic background is not well determined from this data. Flux can be shifted from the soft proton background to the extragalactic background by increasing the energy cutoff (E_c) of the soft proton spectrum, with little change in χ^2. As a result, we kept the normalizations of the extragalactic background fixed. The details of the soft proton - extragalactic background flux exchange did not have a significant effect on the parameters of the thermal components.

4.3. Residual Point Source Contamination

Although the point source removal limit was relatively low, $\sim 10^{36}$ ergs cm^{-2} s^{-1}, it is not sufficiently

[2]http://heasarc.gsfc.nasa.gov/cgi-bin/Tools/xraybg/xraybg.pl

[3]There has been a controversy of whether the Local Hot Bubble exists or whether the emission previously attributed to the Local Hot Bubble is due to heliospheric solar wind charge exchange emission. Without reference to the true source of the emission, at this resolution it can be well fit with an APEC model.

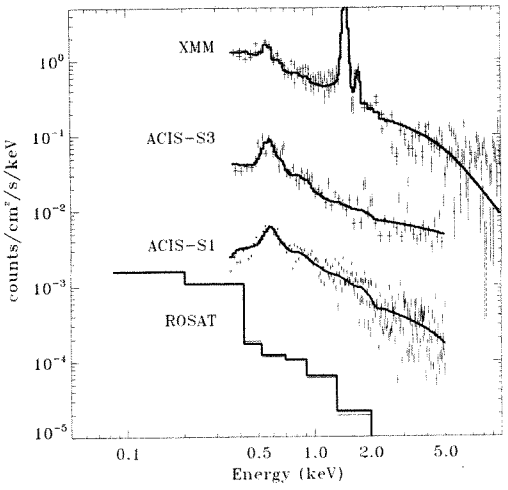

Fig. 9.— The fitted fore/background spectra. The best fit for a given instrument/detector is shown. Since the *ROSAT* data were used only to constrain the other fits, all of the models of the *ROSAT* data produced by the fits to the *Chandra* and *XMM-Newton* data are shown.

TABLE 4
FORE/BACKGROUND FIT PARAMETERS

Parameter	ACIS-S3	ACIS-S1	XMM	ROSAT
Data Parameters				
Exposure (ks)	138.92	597.24	59.89×2	...
Area (am^2)	17.122	70.662	~270	1.0
Source Detection Limit (erg cm^{-2} s^{-1})	1.0×10^{-15}	4.7×10^{-15}	1.3×10^{-14}	4.8×10^{-14}
N_Γ (keV cm^{-2} s^{-1} arcmin^{-2} keV^{-1})	3.47×10^{-7}	3.74×10^{-7}	6.71×10^{-7}	9.13×10^{-7}
Fit Parameters				
kT_L (keV)	$0.103^{+0.003}_{-0.003}$	$0.104^{+0.002}_{-0.003}$	$0.099^{+0.002}_{-0.002}$	...
N_L ($\times 10^{-2}$ cm^{-6} pc)	$2.63^{+0.39}_{-0.41}$	$1.57^{+0.16}_{-0.19}$	$1.55^{+0.37}_{-0.26}$	...
kT_D (keV)	$0.27^{+0.04}_{-0.04}$	$0.27^{+0.04}_{-0.03}$	$0.24^{+0.02}_{-0.02}$	...
N_D ($\times 10^{-2}$ cm^{-6} pc)	$0.329^{+0.089}_{-0.076}$	$0.180^{+0.049}_{-0.034}$	$0.226^{+0.028}_{-0.028}$	...
C_{ROSAT}	$1.08^{+0.17}_{-0.13}$	$1.81^{+0.10}_{-0.09}$	$1.18^{+0.29}_{-0.22}$	...
E_C (keV)	$17.6^{+\infty}_{-10.1}$	∞	$15.6^{+282.}_{-13.0}$	...
N_C ($\times 10^{-2}$ cm^{-6} pc)	$0.047^{+0.021}_{-0.007}$	$0.0072^{+0.0020}_{-0.0022}$	$0.0041^{+0.0019}_{-0.0002}$	...
χ^2_ν	0.87	0.86	1.51	...
ν	89	315	198	...

All errors are 90% confidence intervals. The Galactic absorption in the direction of M101 is 9×10^{19} cm^{-2}

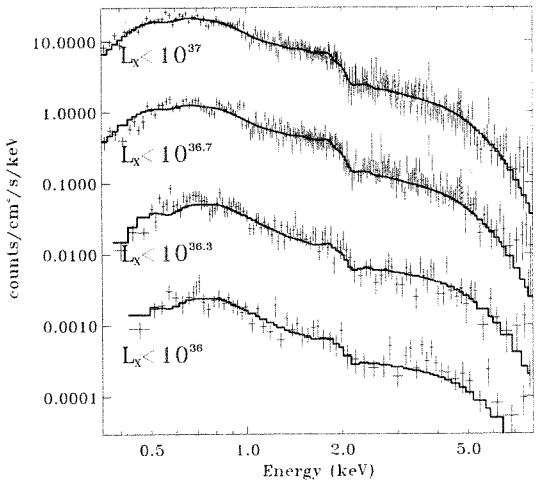

Fig. 10.— The aggregate spectrum of point sources falling within the ACIS-S3 FOV. The ULX in their high state have been excluded. The highest spectrum is all sources with $L_X < 10^{38}$ erg s^{-1}, shifted upwards by 1000, followed by spectra with upper luminosity cutoffs at $L_X < 10^{37}$ shifted upwards by 1000, $L_X < 10^{36.7}$ shifted upwards by 100, $L_X < 10^{36.3}$ shifted upwards by 10 and $L_X < 10^{36}$ erg s^{-1}, unshifted. The fits shown were made simultaneously to the $L_X < 10^{37}$, $L_X < 10^{36.7}$, and $L_X < 10^{36}$ erg s^{-1} spectra, and renormalized to the $L_X < 10^{36}$ erg s^{-1} spectrum. The $L_X < 10^{38}$ erg s^{-1} spectrum requires a significantly different fit.

low to remove all of the X-ray binaries in the galaxy. Thus there will be some residual contamination by unresolved point sources, both in the galaxy and in the background. The spectrum of sources falling within the ACIS-S3 FOV to various limiting fluxes is shown in Figure 10. Given that these spectra are due to aggregates of sources of various spectral shapes, we did not attempt a physically meaningful fit, merely one that described the spectral structure adequately.

The data were extracted from the 85% encircled energy regions described in §2.1. For each source a local background was taken from a concentric elliptical annulus whose inner semi-major axis was twice that of the source region and whose outer semi-major axis was four times that of the source region. The local backgrounds were subtracted from the sources before the various source spectra were summed. The spectra can be fit with a number of different combinations of components. After experimentation, we found that the combination of an absorbed power law and two absorbed black bodies,

$$e^{(\sigma H_\Gamma)} N E^\Gamma + e^{(\sigma H_1)} BB_1 + e^{(\sigma H_2)} BB_2, \qquad (3)$$

described the aggregate spectrum well at all flux levels, with the parameters varying with the flux level. The results are shown in Figure 10.

The residual point source spectrum for the Chandra data was chosen to be that of the sources with $L_X \leq 10^{36.3}$ ergs s^{-1}. (Spectra from sources with $L_X \leq 10^{36.0}$ had too few counts for good spectral fitting, but clearly have an aggregate spectral shape similar to that for sources with $L_X \leq 10^{36.3}$ ergs s^{-1}.) The normalizations were all fixed in relation to that of the

powerlaw, which was allowed to vary. All the other parameters were fixed. It will be noted that this spectrum includes the faint background sources, so the extragalactic power law in Equation 3 and this component are modeling much of the same emission and have similar spectral shapes. If the normalizations of both the extragalactic power law and the residual point source spectrum were allowed to vary, they would be poorly constrained. As a result, we fixed the normalization of the extragalactic power law based on the point source exclusion threshold, and allowed the normalization of the residual point source spectrum to vary. Spectral fits of the global M101 spectrum, excluding the residual point source spectrum and allowing the normalization of the extragalactic background to vary, found that the best fit normalization of the extragalactic background was typically only $\sim 25\%$ higher than the anticipated value. Thus, fixing the extragalactic background normalization to that calculated from the point source exclusion threshold and allowing the normalization of the residual point source spectrum to vary is an adequate representation of the point source spectrum.

4.4. The M101 Spectral Model

The bulk of the ACIS-S3 data in the *Chandra* observing program, the first six observation segments plus obsid 5300, covers approximately the same area, and certainly the same range of radii. Since all of these data were taken over a single year, we have combined these spectra (spectrum M1-M6) with the realization that the absolute normalizations from the spectral fits will characterize a particular mean flux and must be renormalized for any particular region of interest. We have also combined the four observations of the seventh segment into a single spectrum (spectrum M7). The spectrum from the ACIS-S3 chip from obsid 934 (AO-1) was also extracted. Unless otherwise stated, all spectral fits are simultaneous fits of the three spectra described here.

A "background" spectrum, containing only the particle background, was constructed for each spectrum. The responses for each spectrum were created with the standard CIAO tools for creating emission weighted responses, *mkacisrmf* and *mkwarf*.

The M101 Emission Model: We have modeled the emission from M101 as two identical uniform sheets of emission separated by a thin sheet of absorption; two "thick disk/halo" components separated by the absorption of the galactic disk. The functional form of the fit to the M101 emission is

$$AC\left(e^{(\sigma H_{MW})}\right)\left(1+e^{(\sigma H_{M101})}\right)\sum_i (N_i \mathcal{E}(kT_i)) \quad (4)$$

where the A is the area over which the spectrum was extracted. However, the M1-M6, M7, and obsid 934 spectra were extracted from somewhat different regions so their mean surface brightnesses are different, and so C is a compensatory scaling that is set to unity for the M1-M6 spectrum and allowed to vary for the other two spectra. Since the strength of the fore/backgrounds depends on the area A, combining C and A is not useful. H is the column density of neutral hydrogen, and is discussed below. There is a range of possibilities for the actual emission model, $\mathcal{E}(kT_i)$, but in any case it is expected to be thermal and composed of multiple components, each with a temperature kT_i.

The M101 Absorption Model: Setting the strength of the M101 internal absorption is rather difficult. The mean absorption over the inner disk ($0\farcm5 < R < 5\farcm0$) is 1.05×10^{21} cm^{-2}. However, since the X-ray emission is correlated with star-formation, the X-ray emitting sources will be somewhat correlated with the sources of absorption; the X-ray emission weighted mean absorption in the inner disk is 1.14×10^{21} cm^{-2}. For each spectrum we have set the internal absorption to the emission weighted mean absorption for the FOV. This value is fixed in the fit; allowing this value to vary typically results in the internal absorption becoming zero with a corresponding decrease in the emission measures.

Of course, if the absorption is very strongly varying across the field, the resulting spectrum will not be well modeled by a single mean absorption. This is particularly the case when modeling the extragalactic background shadowed by the neutral disk of M101. To understand the extent of this problem, we modeled the transmission of an extragalactic background of the form $E^{-1.46}$ through the neutral hydrogen (as mapped by 21 cm and ^{12}CO) over the region from which the spectra of the M101 diffuse emission had been extracted. We then attempted to fit this modeled absorbed background with a spectrum of the same $E^{-1.46}$ form that had been absorbed by a single column density. For $E \gtrsim 0.45$ keV, the fractional residuals are less than 2%; at 0.35 keV the fractional residuals reach 8%. Since the extragalactic background is small compared to the M101 emission, these errors are acceptable. The value of the absorbing column obtained from these experiments was then used as the absorbing column for the extragalactic background when fitting the M101 spectrum.

The M101 Abundances: For *Chandra* studies of soft thermal emission, the most important abundances are those of the elements that produce the strongest emission: oxygen and iron. The gas-phase oxygen abundance gradient has been studied by Bresolin (2007) and Kennicutt et al. (2003); it is well described by

$$12+\log(O/H) = 8.75(\pm0.05) - 0.90(\pm0.07)R/R_0 \quad (5)$$

where $R_0 = 14\farcm4$. Over the ACIS-S3 FOV, the oxygen abundance ranges from 1.07 solar at $R = 0\farcm5$ to 0.73 solar at $R = 5\farcm9$. The emission-weighted mean oxygen

abundance is 0.75 solar. The gas-phase iron abundance has not been measured. We have set the overall abundance to 0.75 solar and, for the bulk of the fits, we have set the O/Fe ratio to the solar ratio. The solar abundances Wilms et al. (2000) are used throughout.

The Blocking Filter Contamination: From the spectra shown in Figure 11, it is clear that the spectrum from obsid 934 (taken in AO-1) has a very different shape than spectra M1-M6 and M7 for $E < 0.5$ keV. This difference is likely due to the contamination on the optical blocking filter that produces significant absorption at $E < 1.0$ keV. The build-up of the contaminant was quite rapid in the early part of the mission, then slowed and became linear with time (Marshall et al. 2004). The contaminant is not evenly distributed over the blocking filter. Although a correction for the contamination is part of the standard calibration, our comparison is a particularly strenuous test of the calibration; obsid 934 was taken when the time variation of the contamination was quite rapid, the emission of interest is nearly uniform across the field, and the spectrum is at the extreme limits of the bandpass. However, to within the uncertainties, the AO-1 spectrum is consistent with the AO-5 spectra.

4.5. The Global Spectral Fits

The full fit function is the sum of Equations 1 through 4. Both of the parameters describing the soft proton contamination (N_C and E_C from Equation 1) were allowed to vary, and the values for the different spectra were not linked as the soft proton contamination is expected to vary in strength and spectral shape from one observation to another. Of the parameters in Equation 2 (the Galactic foreground and extragalactic background) none was allowed to vary. The response used for the fore/background components was created with the standard CIAO tools assuming uniform emission, which produces a slightly different response than that used for the M101 emission. Of the parameters in Equation 3 (the M101 emission model), all of the area factors, A, were fixed, the scaling factor, C, for the M1-M6 spectrum was fixed to unity, and the column densities (H_{MW} and H_{M101}) were fixed. The M101 abundances were fixed to 75% solar. The other scaling factors were allowed to vary to compensate for the different mean surface brightness contained in the different FOV. The other parameters were allowed to vary, but were required to have the same value for all spectra. Of the parameters in Equation 4 (the residual point source model) only the overall normalization was allowed to vary.

Before fitting the spectrum extracted from the bulk of the galaxy (the global spectrum), some thought must be given to the type of model to be fit, and the use to which the fit parameters are to be put. Any single line of sight through M101 contains multiple emitting components. A typical line of sight contains emission due to the halo or thick disk which, if galactic fountain models are to be believed, is composed of gas expelled from correlated supernovae in star-forming regions. The gas has expanded adiabatically away from the disk and, as a result, should be significantly over-ionized. Conversely, many lines of sight pass through regions of more or less intense star-formation, where the emission is due to colliding winds and cavity supernovae. In these regions the emission should range from under-ionized to nearly in collisional equilibrium.

Compared to a plasma in collisional ionization equilibrium (CIE), an over-ionized plasma will have stronger emission due to high ionization states which means, for a few MK plasma, that the Fe-L complex is stronger compared to O VIII. However, since plasmas at these temperatures have timescales for reaching equilibrium, $10^{11} \lesssim n_e t \lesssim 10^{12}$ cm^{-3} s, whereas the cooling fluence, $n_e t_{cool} \sim 5 \times 10^{13}$ cm^{-3} s, the spectrum will not be strongly different from that of a CIE plasma. This similarity to CIE plasmas is important since over-ionized plasma models are not regularly available through spectral fitting packages. The under-ionized plasmas are more complicated; the spectral region affected and the degree of the effect depends upon on the temperature to which the gas is shocked, and the time since the shock. However, since these models are available through spectral fitting packages, such components can be handled easily. Although each emitting component has a unique set of line ratios, solutions for combinations of these components are not likely to be unique, particularly at the relatively low spectral resolution provided by CCD imaging spectrometers.

With the exception of a spectrum dominated by a highly shocked low-temperature gas, most spectra will be well described by a combination of CIE models. Since, at CCD resolution, fits will not determine the true physical state of the gas, it is not unreasonable to fit a combination of CIE models to describe the distribution of temperatures and emission measures. At best this can be seen as a measure of the emission measure distribution, at worst, as a vector description of the spectral shape useful for comparing spectra from different regions or from different galaxies.

The spectral fitting is also severely constrained by the available spectral resolution. In both the *Chandra* and *XMM-Newton* spectra, the fit is dominated by the O VII/O VIII ratio and the ratio of the oxygen line strength to the strength of the Fe-L complex (the plateau at 0.7 keV $\lesssim E \lesssim$ 1.0 keV), and the energy of the upper edge of that complex. In high signal-to-noise spectra, the temperature of the hotter components is also determined by the small scale spectral structure at the top of the Fe-L complex. The temperature of the cooler components is also determined by the strength of the pseudo-continuum below 0.5 keV. Thus, the num-

ber of spectral features to be fit is rather limited as is, for example, the degree to which one can extract abundance information.

The global spectrum: The "global" spectrum was extracted from the region $0.'5 < R < 5.'0$, excluding the giant H II regions, and consists of spectra extracted from segments M1-M6, M7, and obsid 934 as described above. These three spectra are shown in Figure 11. Since most previous studies of the diffuse emission in late-type spiral disks have fitted the spectra with two thermal components, we began fitting with two APEC thermal models. Fit 1 (Table 5 and panel *a* of Figure 11) produces $(kT_S, kT_H) = (0.2, 0.6)$, similar to several past results for emission from late type disks (see §5.5). The residuals to the fit are small everywhere except below $E \sim 0.5$, where the residual is quite strong, and relatively consistent among the three spectra. This fit, however, is only at a local minimum of χ^2. Fit 2 (panel *b* of Figure 11), $(kT_S, kT_H) = (0.07, 0.3)$, has a better χ^2 than Fit 1, reduces the residual below $E \sim 0.5$, but has stronger residuals above $E \sim 0.7$ keV. Addition of a third APEC component (Fit 3, panel *c* of Figure 11) does a small amount to improve the fit above $E \sim 0.7$ but strong residuals remain below $E \sim 0.5$ keV.

To test the significance of the third CIE component, we simulated 1500 spectra using the best two CIE component model, and fitted each simulation with both a two and a three CIE component model. For the fits to the observed spectra, the difference in χ^2 between the two models is 44.8, while the distribution of $\Delta\chi^2$ for the simulations suggests that values greater than that should occur $< 0.1\%$ of the time. Therefore, the three CIE component model is a better fit to the data, but may not be more physically meaningful.

On the soft excess: That all of the above fits produce strong positive residuals below $E \sim 0.5$ keV suggests a possible problem with either the data, the response, or the background subtraction in this band. Figure 13 shows three spectra extracted from regions with successively higher surface brightness. The spectrum from the lowest surface brightness region is extracted from the largest area while the spectrum from the highest surface brightness region is extracted from the smallest area (see Table 7). If the soft excess were due to a poorly subtracted particle background or a poorly fit Galactic foreground, the spectrum from the lowest surface brightness region should have the greatest soft excess. Instead, the soft excess is most noticeable in the spectra from the higher surface brightness regions.

One can also check the reality of this soft excess by comparing the *Chandra* data and fits to the *XMM-Newton* data. From each of the MOS data sets from each of the three *XMM-Newton* observations we have extracted spectra from $0.' 5 < R < 5.'0$ after excluding sources whose 0.5-2.0 keV *Chandra* luminosities

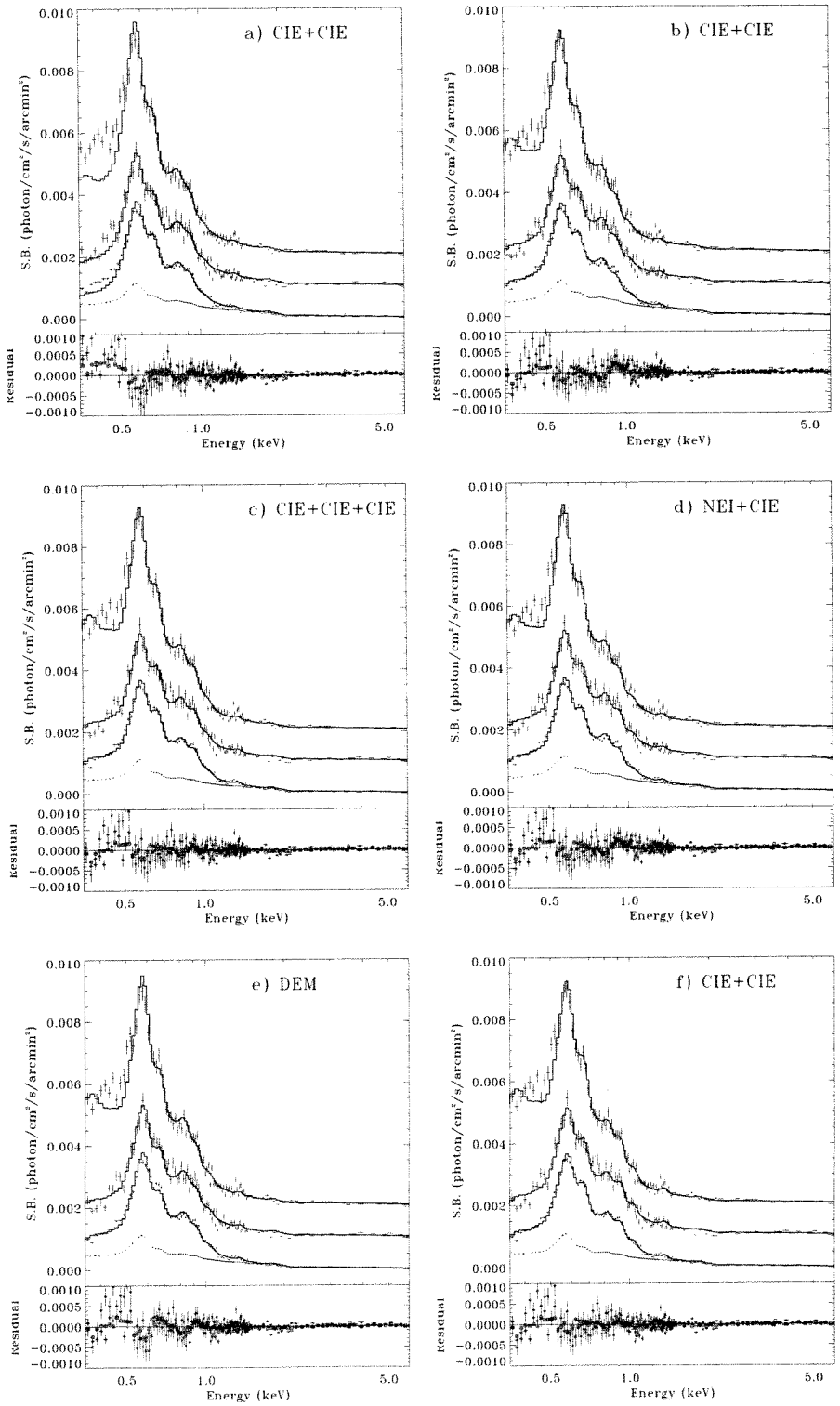

Fig. 11.— Fits to the global spectrum. Each panel contains three spectra *bottom:* from M1-M6, *middle:* from M7 shifted upwards by 0.001, and *top:* from obsid 934 shifted upwards by 0.002. Each spectrum has had the particle background removed. The dotted line is the spectrum from all components not due to the diffuse emission from M101 for the M1-M6 spectrum. The lower plot of each panel shows the difference between the data and the model. The points are coded by spectrum; *boxes:* from M1-M6, *diamonds:* from M7, and *crosses:* from obsid 934.

were greater than 10^{37} erg s$-$1. The particle backgrounds were created and subtracted using the method described in Snowden & Kuntz (2008). The six spectra were fit simultaneously with nearly the same model used with the *Chandra* spectra. Two additional Gaussian components were used to describe the instrumental Al and Si lines. Since the point source exclusion limit was significantly higher than that for the *Chandra* data, the spectrum of the residual point sources was modeled somewhat differently. We used the fit to the aggregate *Chandra* spectrum of all sources with $L_X < 10^{37}$ erg s^{-1} as described in §4.3 to model the sources in the *XMM-Newton* data. The fit parameters derived from the *Chandra* data were applied directly to the *XMM-Newton* data without allowing a renormalization, since the flux of that collection of sources is relatively well measured. (Although the total flux of the population changes with time, a significant change is unlikely.)

Figure 12 shows two reasonable fits to the *XMM-Newton* spectra. For this figure, the individual spectra and the individual models have summed for clarity. The left-hand panel shows a fit (Fit 1X in Table 5) with $(kT_S, kT_H) = (0.20, 0.64)$, similar to Fit 1 of the *Chandra* data. The "soft excess" is clearly seen, so it is not a figment of the *Chandra* calibration. Incidently, nearly the same (kT_S, kT_H) were obtained when assuming no residual point source contribution. The right-hand panel shows a somewhat better fit (Fit 2X in Table 5, $\chi_\nu = 1.17$ *versus* $\chi_\nu = 1.25$ for $\nu = 566$) yielding $(kT_S, kT_H) = (0.07, 0.32)$, similar to Fit 2 of the *Chandra* data. Here the ~ 1 keV residuals do not argue so strongly against this solution due to the relatively short exposure of the *XMM-Newton* observations. In short, correcting for the different point source contamination levels, the *XMM-Newton* and *Chandra* spectra of the inner disk are broadly consistent.

NEI Fitting: That none of the above fits adequately model the data suggests that NEI effects may be important. Consequently, we have modeled the spectrum with a CIE model and an APEC-based under-ionized NEI model. The best fit model of this type produced residuals similar to the two APEC component model (Fit 4, panel *d* in Figure 11). In this case the CIE component had $kT = 0.290^{+0.007}_{-0.007}$ while the NEI component has $kT = 0.123^{+0.009}_{-0.005}$, $\tau = n_e t = (1.88^{+\infty}_{-0.75}) \times 10^{12}$ $cm^{-3}s$. Although this NEI component is not unreasonable, in fact it is similar to the soft CIE component in the best two CIE component fits, it does not improve the fit significantly. A two NEI component model produces nearly the same fit and neither fluence is well determined as both are near their equilibrium values. Thus, NEI components are neither particularly required nor particularly excluded by the data.

Differential Emission Measure (DEM) Fitting: Given that three CIE components are a somewhat better fit to the data than two, it is reasonable to attempt a model with a distribution of emission measures. We have modeled the spectra with a powerlaw distribution of emission measure where the emission at each temperature is represented by APEC models. The powerlaw distribution was characterized by an index (either positive or negative) and both upper and lower temperature cutoffs. The resulting fit (Fit 6, Table 6, panel *e* of Figure 11) had relatively strong residuals, and was not significantly better than the two APEC model. The index of the powerlaw distribution $\alpha = -1.44^{+0.04}_{-0.05}$; the emission measure declines with temperature as one might expect. The fitted temperature limits are consistent with the range of the individual CIE component temperatures found from the previous fits.

Using the ROSAT spectrum to constrain the fits: The low temperature components found in the three CIE component fit and the DEM fit should produce significant flux below the *Chandra* bandpass. The *ROSAT* bandpass extends down to 0.11 keV. However, given the relatively poor spatial resolution of the PSPC camera, point source removal is not feasible. Thus the *ROSAT* SED contains not only the diffuse emission from M101 but also the point source emission as well. Although we have modeled the spectrum of the point sources, the extent to which that spectrum can be extrapolated through the remainder of the *ROSAT* band is not clear. Thus, the *ROSAT* spectrum provides only a weak constraint.

We have fitted the three *Chandra* spectra used in the above fits simultaneously with the *ROSAT* spectrum from the same region. Since the Galactic foreground and the extragalactic background have already been removed from the *ROSAT* spectrum, those components were not included in the fit to the *ROSAT* spectrum. The point source contribution in the *ROSAT* spectrum was modeled using the spectrum of all of the point sources that were not in a ULX state within $0.'5 < R < 5.'0$ and with S/N> 3 in the 0.5-2.0 keV band. The normalization of the model of the diffuse M101 emission for the *ROSAT* spectrum was allowed to vary in the same way that the relative normalizations of the three *Chandra* spectra were allowed to vary.

The *ROSAT*-constrained versions of the two and three CIE component model fits (Fit 2R *versus* Fit 2 and Fit 3R *versus* Fit 3) produced nearly the same parameters as the unconstrained fits. In neither case did the fits overproduce flux in the *ROSAT* R1 and R2 bands ($0.111 < E < 0.284$ keV). Given the increase in emission measure as kT decreases, the DEM model should be particularly sensitive to the *ROSAT* constraint. However, comparison of the fits with and without the *ROSAT* constraint (Fit 6 *versus* Fit 6R, both in Table 6) show no significant differences. Thus, the *ROSAT* data do not significantly constrain the fits.

Fitting abundances Given the arguments above about the limited number of spectral features, fitting

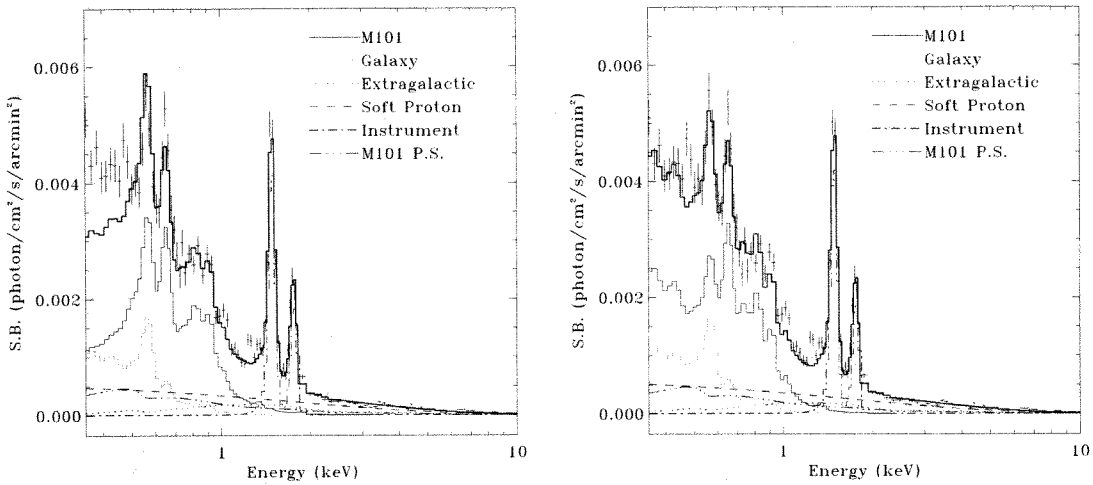

Fig. 12.— Two fits to the *XMM-Newton* spectra extracted from $0.5' < R < 5.0'$ after excluding sources whose 0.5-2.0 keV *Chandra* luminosities were greater than 10^{37} erg/s. **Left:** A fit with $(kT_S, kT_H) = (0.20, 0.64)$ and $\chi_\nu = 1.25$. **Right:** A fit with $(kT_S, kT_H) = (0.07, 0.32)$ and $\chi_\nu = 1.17$. In both panels the model is the thick solid line. The model is decomposed into its components as shown in the legend. The point source component is the difference between the point sources excluded from the *XMM-Newton* spectra and those excluded from the *Chandra* spectra.

TABLE 5
GLOBAL SPECTRUM: FIT PARAMETERS I

	Model	kT_S (keV)	kT_I (keV)	kT_H (keV)	N_S (10^{-2} cm^{-6} pc)	N_I (10^{-2} cm^{-6} pc)	N_H (10^{-2} cm^{-6} pc)
Fit 1	apec+apec	$0.187^{+0.003}_{-0.003}$	...	$0.584^{+0.019}_{-0.020}$	$1.515^{+0.009}_{-0.009}$	...	$0.257^{+0.011}_{-0.019}$
Fit 2	apec+apec	$0.113^{+0.003}_{-0.002}$	...	$0.292^{+0.005}_{-0.005}$	$2.572^{+0.142}_{-0.134}$	...	$0.922^{+0.042}_{-0.038}$
Fit 2R	apec+apec+rosat	$0.109^{+0.003}_{-0.002}$	...	$0.290^{+0.006}_{-0.006}$	$2.891^{+0.134}_{-0.154}$	...	$0.944^{+0.043}_{-0.047}$
Fit 2A	apec+apec	$0.115^{+0.003}_{-0.003}$	...	$0.327^{+0.009}_{-0.009}$	$2.625^{+0.146}_{-0.146}$	...	$1.101^{+0.042}_{-0.042}$
Fit 2E	apec+apec	$0.203^{+0.004}_{-0.003}$	...	$0.608^{+0.020}_{-0.018}$	$1.308^{+0.028}_{-0.035}$	...	$0.258^{+0.016}_{-0.012}$
Fit 3	apec+apec+apec	$0.112^{+0.002}_{-0.003}$	$0.279^{+0.009}_{-0.005}$	$0.812^{+0.082}_{-0.096}$	$2.643^{+0.014}_{-0.023}$	$0.929^{+0.053}_{-0.053}$	$0.077^{+0.030}_{-0.023}$
Fit 3R	apec+apec+apec	$0.111^{+0.002}_{-0.002}$	$0.278^{+0.008}_{-0.008}$	$0.817^{+0.082}_{-0.100}$	$2.711^{+0.013}_{-0.020}$	$0.929^{+0.054}_{-0.055}$	$0.079^{+0.020}_{-0.023}$
Fit 4	nei+apec	$0.123^{+0.009}_{-0.005}$	...	$0.290^{+0.007}_{-0.007}$	$2.398^{+0.292}_{-0.509}$	$1.259^{+0.117}_{-0.144}$	$1.259^{+0.112}_{-0.144}$
		$\tau = (1.887^{+\infty}_{-0.750}) \times 10^{12}$					
Fit 5	nei+nei	$0.115^{+0.003}_{-0.005}$	...	$0.295^{+0.004}_{-0.004}$	$2.257^{+0.164}_{-0.210}$	...	$0.927^{+0.047}_{-0.040}$
		$\tau = 2.881 \times 10^{13}$		$\tau = 5.000 \times 10^{13}$			
				XMM-Newton Fits			
Fit 1X	apec+apec	$0.204^{+0.010}_{-0.010}$	...	$0.651^{+0.522}_{-0.047}$	$1.551^{+0.093}_{-0.095}$	...	$0.305^{+0.038}_{-0.060}$
Fit 2X	apec+apec	$0.071^{+0.008}_{-0.008}$	...	$0.282^{+0.010}_{-0.008}$	$13.83^{+4.77}_{-6.67}$	...	$1.350^{+0.104}_{-0.087}$

abundances would not seem to be a particularly useful exercise. We have limited our study of the abundances in M101 to two relatively tractable problems.

Although the gas phase abundance of oxygen is well measured in the optical, there is no information about some of the primary X-ray emitting elements, such as iron. We linked the abundances of the light elements (He, C, and N) and the alpha process elements (Ne, Mg, Al, Si, S, Ar, and Ca) to that of oxygen. The abundances of iron and nickel were linked, and allowed to vary with respect to oxygen. We then fit the spectra with a two CIE component model (Fit 2A and panel *f* of Figure 11). The iron abundance fell to roughly 60% that of oxygen, the temperature of the soft component did not change significantly while the temperature of the harder component increased. The main reason that a two component fit works better for variable abundances than for fixed abundances is that varying the (Ne,Mg)/Fe allows a better fit to the 0.82 and 0.95 keV features with a single temperature. A similar three CIE component fit was not significantly better, the iron abundance again fell to roughly 60% that of oxygen, but the lowest temperature component became very poorly constrained.

Having fixed [O/H] to -0.12, we found [Fe/H]=-0.37, implying [O/Fe]=0.24. From the models and data

TABLE 6
GLOBAL SPECTRUM: FIT PARAMETERS II

(keV)	Model	kT_S (keV)	α	kT_H	χ_ν	ν	Comment
Fit 6	powdem	$0.013^{+0.003}_{-0.003}$	$-1.443^{+0.042}_{-0.048}$	$0.740^{+0.034}_{-0.024}$	1.358	374	
Fit 6R	powdem+rosat	$0.006^{+0.010}_{-0.006}$	$-1.445^{+0.045}_{-0.052}$	$0.761^{+0.044}_{-0.044}$	1.436	380	

shown in Chiappini et al. (2003) and references therein, this value of [O/Fe] is consistent with the [O/Fe] to [Fe/H] relation for solar neighborhood stars. Chiappini et al. (2003) further show that the [O/H], [C/O], and [N/O] gradients in M101 are consistent with those derived using their Milky Way model, suggesting that the [Fe/H] relation should be similar. Conversely, there are a number of uncertainties, possible systematic uncertainties in fitting the X-ray data, the [O/H] was measured from H II regions while the [Fe/H] is fitted from the X-ray emission (which may be more processed material), and both of the abundances are measured over a wide range in radii (and thus potentially very different star formation histories). None the less, the model obtained by allowing [Fe/H] to float suggests that the lower iron abundance is not unreasonable.

The soft excess below E$\sim$ 0.5 keV might also be due to incorrect model abundances. A fit using two CIE components with the addition of a Gaussian to model the soft excess found that the addition of a line with $kT \sim 0.48$ keV and $\Delta kT \sim 0.1$ keV produced a reduced χ^2 of slightly less than unity with no strong residuals at any energy. This fit suggests that the soft excess might be due to an over-abundance of carbon and nitrogen, both of which have significant emission in this band compared to the remainder of the spectrum. Linking the carbon and nitrogen abundances, setting all the other abundances to that of oxygen, and fitting, produced carbon and nitrogen abundances roughly three times solar (Fit 2E). This value is unreasonably high given the work of Chiappini et al. (2003).

Residual Point Sources: For the three CIE component fit, the residual point-source emission accounts for $\sim 4\%$ of the total M101 emission. The two component fits allowed slightly higher amounts.

4.6. Surface Brightness Fits

The increase of hardness ratio with surface brightness could be due to changes in either emission measure or temperature. To understand the underlying spectroscopic cause of the variation of the hardness ratio, we extracted spectra from regions defined by three surface brightness levels, again excluding the regions around the bulge and the giant H II regions. The three spectra are shown in the left panel of Figure 13, while the regions from which they were extracted are shown by the dark contours of the middle panel of Figure 13. The spectra were extracted from the M1 through M6 obsids only. The spectra were fitted over the more restricted range of 0.45 keV<E<10.0 keV in order to avoid the complication of the soft excess discussed above, and to produce a fit that corresponds to the hardness ratio that was measured. The spectra were fitted assuming the emission-absorption-emission geometry where the emission was modeled by two APEC components. The mean absorption was calculated in the same manner as for the global spectrum. Fits to each of the spectra individually produced consistent temperatures to within the uncertainties. A simultaneous fit of the three spectra was then used to determine the relative emission measures, which are plotted in the right panel of Figure 13. For these three spectra, the ratio of the emission measures, N_H/N_S, increases with surface brightness.

Dividing the intermediate surface brightness region into four bins with narrower ranges of surface brightness shows a similar result, but there is one strongly discrepant data point. Careful examination of the color map for this surface brightness interval, and subdivision of the region did not reveal any apparent cause for the discrepancy, though the spectral shape of the Fe-L complex for this region was very different from those of the other spectra. Thus, while the emission measure of the harder component increases with respect to the softer as the surface brightness increases, that relation may break down on smaller scales.

We have attempted to extend this analysis down to 0.35 keV using a three CIE component fit. The results are equivocal since the three components do not map cleanly onto the two bands used for the hardness ratio. However, such an analysis does suggest that the softest component, which does the most to account for the soft excess, decreases compared to the $\sim$0.25 keV component as the surface brightness increases.

One might suspect that the increase of the N_H/N_S ratio with surface brightness is due to a relatively uniform faint component, (a halo for example) with one ratio, and a second component of variable strength (star-formation) with a different ratio. However, that the second derivative of the function is positive (including the data from the giant H II regions) or roughly zero (excluding those data) excludes that possibility; the variable component would have to have a N_H/N_S

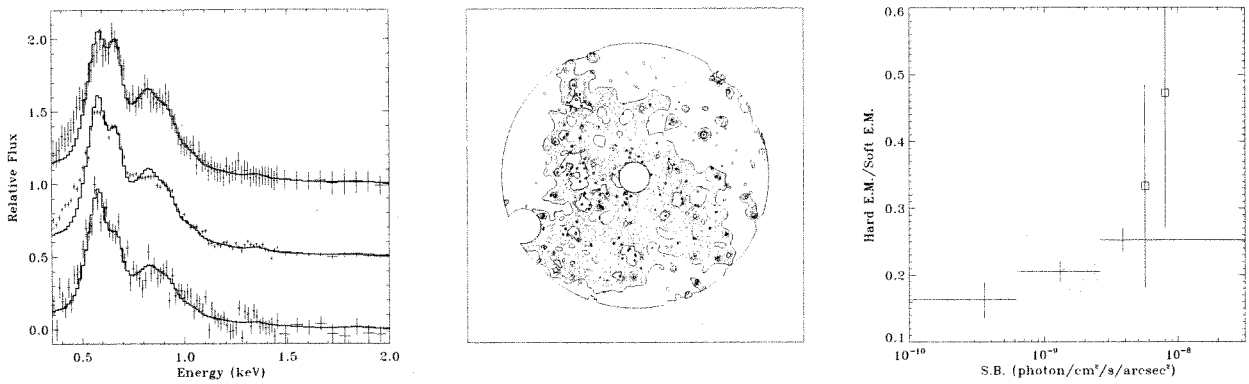

Fig. 13.— **Left:** Spectra extracted from regions with successively higher surface brightnesses. The three spectra were extracted from regions with $SB < 8.3 \times 10_{16}^{-10}$ and $R < 5'.0$, $8.3 \times 10_{16}^{-10} < SB < 2.6 \times 10_{8}^{-9}$, and $2.6 \times 10_{8}^{-9} < SB$. The subscripts indicate the σ in 0".492 pixels of the Gaussian smoothing used for the surface brightness image. **Middle:** Countour map showing the regions from which the spectra were extracted. The contours are $8.3 \times 10_{16}^{-10}$, $1.0 \times 10_{8}^{-9}$, $1.5 \times 10_{8}^{-9}$, $1.8 \times 10_{8}^{-9}$, and $2.6 \times 10_{8}^{-9}$. **Right:** The ratio of the emission measures of the two fitted components for each of the spectra. The intermediate surface brightness bin can be broken into four, which are also plotted here.

TABLE 7

SURFACE BRIGHTNESS SELECTED SPECTRA: FIT PARAMETERS

Extraction Region	Counts[a]	Area (arcmin^2)	N(H)	S.B.[b] 10^{-10} sbu	N_S	N_H	N_H/N_S
$kT_S = 0.192^{+0.128}_{-0.001}$ $kT_H = 0.601^{+0.404}_{-0.015}$ (3 spectra)							
BRT	10330	2.71	1.83	38.4	$11.24^{+0.52}_{-0.37}$	$2.87^{+0.15}_{-0.24}$	0.255 ± 0.020
MID	52697	32.8	1.64	13.0	$4.05^{+0.19}_{-0.13}$	$0.830^{+0.065}_{-0.053}$	0.204 ± 0.017
DMR	19392	28.4	1.26	3.56	$1.13^{+0.05}_{-0.04}$	$0.187^{+0.03}_{-0.033}$	0.165 ± 0.028
$kT_S = 0.194^{+0.176}_{-0.003}$ $kT_H = 0.601^{+0.559}_{-0.017}$ (6 spectra)							
BRT	10330	2.71	1.83	38.4	$11.27^{+0.25}_{-0.38}$	$2.84^{+0.17}_{-0.21}$	0.252 ± 0.018
IND	10510	4.28	1.74	23.8	$7.48^{+0.16}_{-0.25}$	$1.44^{+0.20}_{-0.18}$	0.192 ± 0.027
INC	12011	6.04	1.65	18.6	$5.86^{+0.13}_{-0.20}$	$1.04^{+0.14}_{-0.14}$	0.177 ± 0.025
INB	13524	8.07	1.60	14.0	$4.40^{+0.10}_{-0.15}$	$0.810^{+0.114}_{-0.117}$	0.183 ± 0.026
INA	17122	14.7	1.59	7.26	$2.15^{+0.05}_{-0.07}$	$0.560^{+0.049}_{-0.049}$	0.268 ± 0.024
DMR	19392	28.4	1.26	3.56	$1.14^{+0.02}_{-0.04}$	$0.185^{+0.029}_{-0.032}$	0.163 ± 0.027

[a]The number of counts in 0.35 keV $< E <$ 10.0 keV after the subtraction of the particle background.

ratio that increases with the component strength.

The Giant H II Region Spectra: The giant H II regions NGC 5461 and NGC 5462 represent the highest surface brightess regions. The spectra were extracted from within the 2.6×10^{-9} sbu contour around each giant H II region. Due to the relatively small number of counts, all of the spectra from the M1 through M7 segments were combined, and fit simultaneously with the spectrum from obsid 934. The spectra were fit over 0.35 keV $< E <$ 10.0 keV with two CIE component models (Figure 14). The fitted temperatures (Table 8) are consistent with the $(kT_S, kT_H) \sim (0.2, 0.6)$ rather than the $(kT_S, kT_H) \sim (0.1, 0.3)$ solution. Indeed, one can see quite clearly the lack of a strong soft excess in both of these spectra. Despite the relatively low signal to noise, the spectra from the two giant H II regions show different O VII/O VIII and O-line/Fe-L complex ratios, which are reflected in the fitted temperatures; NGC 5461 is hotter (and brighter) than NGC 5462. This result is interesting as NGC 5462 famously shows a large H I cavity and evidence of an outflow (Kamphuis et al. 1991), while NGC 5461 shows a concentration of H I gas and no clear evidence for an outflow. It is suggestive that the X-ray emitting plasma in NGC 5461 may experience greater pressure confinement than the X-ray emitting plasma in NGC 5462 which may be able to expand into a void in the neutral gas. Similarly, we may be seeing evolutionary effects in that the plasma in NGC 5462 has expanded and cooled, whereas NGC 5461 may not have broken out. The N_H/N_S ratios

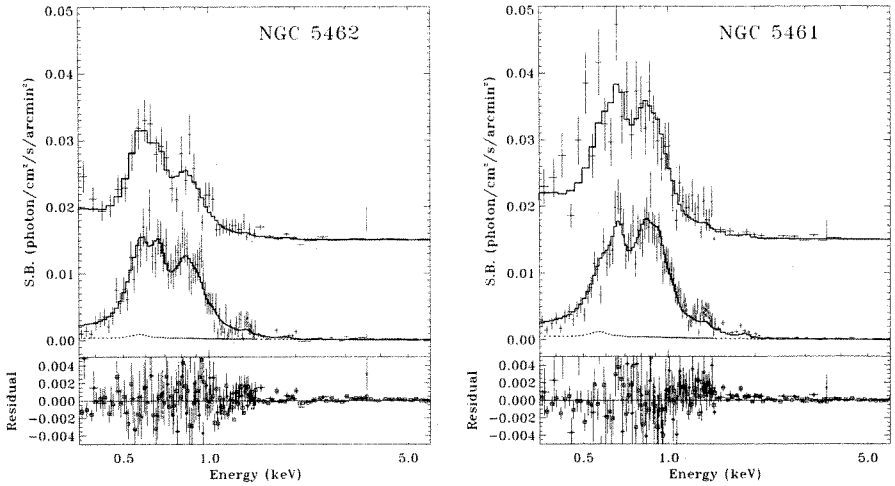

Fig. 14.— Each panel contains two spectra. The *bottom* spectrum is from M1-M7 while the *top* spectrum is from obsid 934 shifted upwards by 0.015 sbu. The dotted line shows the non-M101 contributions to the spectrum. **Left:** Spectra of NGC 5461. **Right:** Spectra of NGC 5462.

of the two giant H II regions are plotted as boxes in Figure 13.

The Bulge Spectrum: The bulge spectrum was extracted from within the 2.6×10^{-9} sbu contour and fit in a similar manner. The spectra are better fit by the $(kT_S, kT_H) \sim (0.1, 0.3)$ solution, more similar to the bulk of the emission. There is some evidence for the soft excess, but the number of counts is insufficient for more detailed fitting. We suggest that while the bulge has a surface brightness similar to that of NGC 5462, the emission mechanisms are more similar to that of the bulk of the disk rather than like the more extreme environment of the giant H II regions. It is probably not dominated by star-formation, and the HST images do not show a large population of young stars in the bulge.

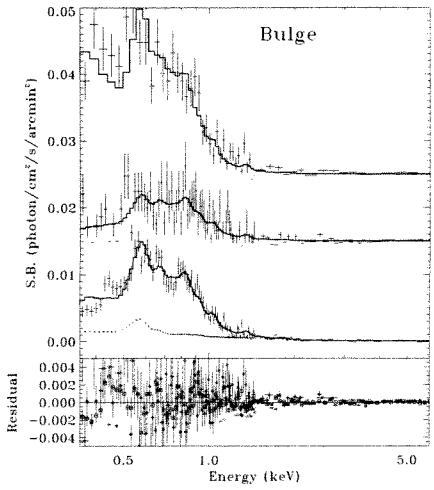

Fig. 15.— Spectra for the bulge. The *bottom* spectrum is from M1-M6, the *middle* spectrum is from M7 shifted upwards by 0.015 sbu, while the *top* spectrum is from obsid 934 shifted upwards by 0.025 sbu. The dotted line shows the non-M101 contributions to M1-M6 spectrum.

4.7. Spectroscopic Summary

The global spectrum of the diffuse emission in M101 is not well fit by any model, with the greatest discrepancy below $E \sim 0.5$ keV. The best fit models contain either three CIE components with fixed abundances, or two CIE components if the iron-group abundances are allowed to vary. The spectra selected on the basis of surface brightness suggest that there is no systematic change in the temperatures of the components as a function of surface brightness, perhaps due to being the average over many different regions. The ~ 0.2 keV component increases with surface brightness, while the ~ 0.6 component increases with respect to the ~ 0.2 keV component. The behavior of the soft excess/softer component with surface brightness is not clear but appears to decline with respect to the ~ 0.2 keV component as the surface brightness increases.

5. Discussion

5.1. The Sources of the Diffuse Emission

It has long been understood that the dominant source of the total X-ray emission in late-type spirals must be star-formation; the L_X derived from *Einstein*

TABLE 8
SPECTRA FROM SELECTED REGIONS: FIT PARAMETERS

Name	Counts[a]	kT_S keV	kT_H keV	N_H/N_S	χ^2_ν	ν
NGC 5462	1790	$0.206^{+0.027}_{-0.021}$	$0.602^{+0.096}_{-0.085}$	0.333 ± 0.152	0.514	187
NGC 5461	2832	$0.258^{+0.051}_{-0.050}$	$0.721^{+0.093}_{-0.113}$	0.472 ± 0.204	0.493	186
BULGE	4345	$0.097^{+0.013}_{-0.009}$	$0.346^{+0.029}_{-0.024}$	0.202 ± 0.074	1.158	310

[a]The number of counts in 0.35 keV $< E <$ 10.0 keV after the subtraction of the particle background.

studies is more strongly correlated with L_{FIR}, an indicator of the star-formation rate, than with L_H, a tracer of the total stellar mass, while the reverse is true in early-type spirals (Fabbiano & Shapley 2002, and references therein). The earliest highly-smoothed *Chandra* images of spiral galaxies showed the X-ray emission to be correlated with spiral arms, and thus with star-formation (e.g. Tyler et al. 2004). The object of this study was to obtain a sufficiently deep exposure that one could identify individual X-ray-emitting structures, such as superbubbles or large OB complexes. To some extent this has been accomplished; Figures 4 and 5 show clear relations between individual X-ray knots and individual H II regions and star-forming complexes.

Although it is clear that the bulk of the diffuse X-ray emission is related to star-formation, it remains to quantify what fraction of the X-ray emission is not due to star-formation. The X-ray emission clearly extends beyond the sites of strong star-formation, so it remains to be qualified how much of the emission is due to current star formation, stellar wind and supernova blown bubbles, and how much of the emission is due to less recent star formation, the non-localized diffuse emission. Unresolved X-ray binaries account for only $\sim 4\%$ of the observed emission (§4.5). The following section first determines the amount of X-ray emission due to identifiable SNR. We then use the radial profiles in the X-ray and FUV to place a limit on the amount of X-ray emission due to stars. We then show that the shape of the X-ray/FUV correlation can be understood by a fairly simple model of young stellar clusters.

Individual SNR: One can estimate the fraction of the diffuse emission due to optically identifiable SNR. The Matonick & Fesen (1997) catalogue of SNR in M101 was created by searching for objects with large [S II]/Hα ratios in ground-based images. Due to resolution and confusion, such a catalogue primarily misses small faint remnants and remnants without strong [S II], which also tend to be young and small. Such remnants, if X-ray bright, would have been excluded as point-like sources. For each SNR in the Matonick and Fesen catalogue, we created a region with a radius equal to the square root of the sum of the squares of the quoted semi-major axis and the PSF size, but no smaller than 5″. We then measured the surface brightness within the SNR regions; the Matonick and Fesen remnants account for a total of $\sim 3.3\%$ of the 0.45-1.0 keV flux within the ACIS-S3 mosaic while occupying $\sim 1.2\%$ of the area in that mosaic. Only a dozen of the Matonick and Fesen remnants are coincident with strong X-ray knots with surface brightness $> 2 \times 10^{-9}$ sbu. All in all, the optically identifiable SNR make a minor contribution to the total diffuse X-ray emission. Although the bulk of the X-ray emission may be created by supernovae the emission must be from supernovae that have lost their identities and are no longer distinguishable as individual remnants.

FUV Emission and Its Timescale: The X-rays due to current star formation are produced by supernovae and, to a much lesser extent, winds from massive stars. Thus, these X-rays should be correlated with tracers of massive star formation. The FUV emission sampled by the *GALEX* FUV band is due primarily to massive stars; $\sim 75\%$ is due to O stars with $M_{init} > 25\ M_\odot$ and $\sim 95\%$ is due to O and B stars with $M_{init} > 8\ M_\odot$ for a zero-age stellar population. Thus the bulk of the FUV emission is produced by the stars that will produce the X-rays.

There are two FUV time-scales of interest; the average age of the stars emitting in the FUV, and the average age of star-forming regions emitting strongly in the FUV. From the Padova isochrones (Marigo et al. 2008), the flux weighted average age for a simple stellar population (SSP) is ~ 32 Myr, roughly the main-sequence lifetime of a $8M_\odot$ star. This age is due to the large number of low mass stars that produce $\lesssim 5\%$ of the peak FUV emission, but produce that amount for a very long time. Conversely, if one considers a star-forming region with a maximum stellar mass of $\sim 60M_\odot$, and assume that the region becomes indistiguishable from the background when it has faded to 5% of its peak FUV brightness, then the average age of the FUV bright star-forming regions is only ~ 7 Myr, roughly the age of a $26M_\odot$ star. These time-scale considerations are important when looking at the correlations over small scales; FUV identifiable star-forming regions should fade much

more quickly than their X-ray emission, possibly leaving X-ray "fossil" star-forming regions. Although the FUV/X-ray emission ratio changes with the age of the stellar population the large scale FUV/X-ray correlation should be dominated by FUV emission from stars formed in the last $\sim$ 10 Myr and the X-ray emission from stars formed between 2 and 32 Myr ago. The latter should be extended to even older ages to account for the cooling time of the hot plasma. Thus, the large scale FUV/X-ray correlation reflects the ratio of current to recent star-formation, though in a relatively complex way.

5.2. Radial Profile

Figure 16 shows the radial profiles of the X-ray and absorption-corrected FUV emission normalized in the 1′ <R< 3′ annulus. Save for the inner arcminute, the correspondence is quite close, suggesting that the bulk of the X-rays are related to current and recent star formation. However this correspondence should not be taken too far as there is, cumulatively, a significant amount of FUV emission from lower mass stars (20% of the flux is due to stars older than 20 Myr) which also produce X-rays but with a different FUV/X-ray ratio.

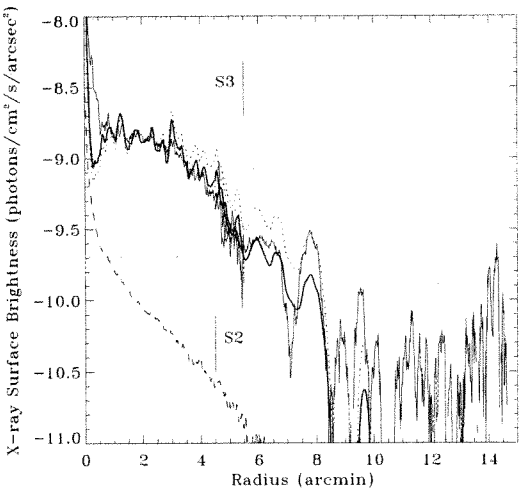

Fig. 16.— The surface brightness profile. *Solid:* The 0.45-1.0 keV band from the ACIS-S3 and ACIS-S2 detectors, which overlap from 4′.5 to 5′.5. The ACIS-S3 profile has been smoothed by 1″.5 while the ACIS-S2 profile has been smoothed by 11″.3. *Dotted:* The *GALEX* FUV emission normalized to the X-ray at 1′ <R< 3′. Note that it rises significantly above the X-ray emission at large radii. The profile has been smoothed to match the X-ray data at the same radius. *Grey:* The *GALEX* FUV emission corrected for extinction and normalized to the X-ray at 1′ <R< 3′; it appears to track the X-ray quite well to R$\sim$ 12′. *Dashed:* The expected X-ray emission from chromospherically active dwarfs calculated from the K band profile.

The most direct estimate of X-ray emission due to stars scales the K-band luminosity which is generally used to trace the total stellar mass. The problem is that the X-ray luminosity function and X-ray spectrum for stars is poorly characterized. Revnivtsev et al. (2007) has attempted to solve this problem using X-ray observations of M32 and, assuming that there is no diffuse X-ray emitting gas in that galaxy, finds that:

$$L_{2.0-10.0} = (3.3 \pm 1.0) \times 10^{27} L_{K_S} \mathrm{erg\ s^{-1} L_\odot^{-1}}. \quad (6)$$

We extracted a K band image of M101 from the 2Mass Large Galaxy Atlas[4] (Jarrett et al. 2003), created a radial profile, and used the Revnivtsev scaling to obtain the 2-10 keV X-ray emission due to stars. The stellar spectrum described in Revnivtsev et al. (2007) has two thermal components; kT = 1.0 keV with abundance z = 0.03, and a second with kT = 5.0 keV and solar abundance. The relative normalizations are not given, but the spectrum shown in Revnivtsev et al. (2007) has two components that cross at E = 1.4 keV, which requires the harder component to have a normalization that is 0.45 times that of the softer component. We used this spectral model to convert from the 2-10 keV emission to the 0.45-1 keV emission, and the result is shown as the dotted line in Figure 16. The uncertainties are neccessarily large given the need to extrapolate from one broad energy band to another. The stellar fraction rises from $\sim$ 10% in the nucleus to $\lesssim$ 15% at R= 0′.5, then declines to $\sim$ 5% at 3′, and remains at that level to at least 5′. The radial profile of the stellar emission is much steeper than the radial profile of the diffuse emission. Given the hardness of the Revnivtsev spectrum, the stellar contribution must be relatively small else one would see a change in X-ray hardness ratio with radius. However, there are two problems with applying this relation to M101.

First, the Revnivtsev scaling is appropriate only for an old stellar population as the younger stellar population will have a higher K-band luminosity, and younger stars have higher X-ray luminosities. G, K, and M stars in the 0.1-1 Gyr range are an order of magnitude more luminous in the X-ray than the stars in the 1-10 Gyr range; with a continuous star formation rate the 0.1-1 Gyr sample produces as much X-ray emission as the 1-10 Gyr sample (see Kuntz & Snowden 2001, and references therein). Thus, the stellar X-ray emission in M101 should be two to three times greater per mass than in M32. The K band flux for the entire stellar population, conversely, declines by a factor of 30 from 0.01 Gyr to 0.1 Gyr, by a factor of four between 0.1 Gyr and 1.0 Gyr, and by another factor of four between 1.0

[4]http://irsa.ipac.caltech.edu/applications/2MASS/LGA/

Gyr and 10.0 Gyr (Vázquez & Leitherer 2005) Thus the Revnivtsev et al. (2007) scaling may be off by factors of two to ten, depending upon the strength of the youngest population.

Second, the Revnivtsev spectrum is incomplete. The stellar SED used by Kuntz & Snowden (2001) was determined from two component fits of *ROSAT* spectra of stars and was described by two thermal components with $kT \sim 0.15$ keV and $kT \sim 0.8$ keV. A large number of studies find the aggregate spectrum of stars in massive star-forming regions to have $kT_S \sim 0.2$ keV and kT_H =1-3 keV (e.g., Franciosini et al. 2005; Townsley et al. 2003, and others). Thus, the Revnivtsev spectrum should probably be augmented by another softer component. The relative strength of the component is not clear as the ratio of the emission measures for the young stars are typically not well characterized. Kuntz & Snowden (2001) suggested that the 0.2 keV component was small compared to the 0.8 keV component.

Given its spectral shape, the Revnivtsev stellar contribution is similar to the aggregate X-ray point source spectrum, so meaningful simultaneous spectral fitting of these two components is not possible. Replacing the X-ray point source model with the Revnivtsev stellar model, one finds that the Revnivtsev model can account for only $\sim 2\%$ of the diffuse emission. Addition of the softer component should not increase this amount substantially.

5.3. The X-ray/FUV Correlation

The amount of emission not related to star formation: The global FUV/X-ray correlation is shown in the left panel of Figure 17. Both the FUV and X-ray data were binned by the FUV surface brightness after the removal of foreground stars. The correlation is shown both including and excluding the bulge and the giant H II regions. The soft X-ray surface brightness is a strong non-linear function of the FUV surface brightness over two orders of magnitude in FUV surface brightness and over one order of magnitude in X-ray surface brightness. This correlation suggests that the bulk of the X-ray emission is indeed the product of star-formation. The giant H II regions show a stronger relation at higher FUV surface brightnesses than does the remainder of the disk. The relation for the remainder of the disk can be roughly described by the function

$$\Sigma_X = A + B\Sigma_{FUV}^{\beta} \quad (7)$$

for FUV surface brightnesses below 0.08 sbu. One must be careful interpreting the relation at $FUV > 0.08$ sbu, as each data point above that value is the average of only a few individual star-forming regions while data points below that value are the average of many regions.

Given that global correlation for the bulk of the disk seems to be different from that including the giant H II regions, one may ask whether the correlation is universal. One could imagine that due to the decrease of the surface density of molecular gas (not yet measured for this galaxy), or the strong radial dependence of the abundances, that the nature of star formation might change with radius. We divided the disk into a number of annular zones and repeated the analysis; the results are seen in the bottom panel of Figure 17. The correlations for individual annular regions show progessively lower X-ray surface brightness at a given FUV surface brightness as one moves outward in the galaxy.

We fitted Equation 7 to the data for each annulus. The initial fit allowed all parameters to vary for all radii (the top third of Table 9). The X-ray offset, A, became negative for the outer two radii, so subsequent fits constrained $A \geq 0$, producing the fitted curves shown in the bottom panel of Figure 17 (the middle third of Table 9). In all cases, β is slightly larger than 0.5, and that there is no significant trend in B with radius. Fixing the exponent to the average, 0.55, and fitting, A decreases with radius, but there is no signifcant trend in B. The X-ray offset, A, is roughly 20% of the X-ray surface brightness in the 1.″0 <R< 3.″0 annulus, $\lesssim 10\%$ of the X-ray surface brightness in the 3.″0 <R< 4.″0 annulus, and is not significant in the 4.″0 <R< 5.″0 annulus. This offset represents X-ray emission that is not due to the recent star-formation traced by the FUV flux. This emission may be due to X-ray disk emission from star-formation older than $\sim$ 20 Myr whose FUV emission is faint, to an extended bulge/halo, and to emission from chromospherically active dwarf stars.

The shape of the correlation itself: Assuming a simple stellar population, one can calculate the supernova rate from the initial mass function and the main-sequence lifetime. Using the Girardi isochrones (Marigo et al. 2008)[5] one finds that the FUV emission is relatively constant before the first supernovae, and then drops rapidly upon the onset of supernovae due to the strong mass-luminosity relation and the increase in surface temperature with mass. For a collection of identical star clusters, each of which contains a simple stellar population (SSP), the FUV brightest ones will have little to no X-ray emission, while the FUV fainter clusters will have stronger X-ray emission.

The "×" symbols in the left panel of Figure 17 plot the data for individual FUV knots whose surface brightnesses are above ~ 0.08 sbu, an approximate "confusion limit". The *HST* image shows each of these FUV knots to be composed of either an individual H II region or a small collection of H II regions. The FUV/X-ray relation for the FUV knots is much steeper than the global relation. The small boxes plot the data for individual X-ray knots whose surface brightnesses are above $\sim 2.6 \times 10^{-9}$ sbu. These X-ray knots tend to be ex-

[5]Available from http://stev.oapd.inaf.it/cgi-bin/cmd_2.2.

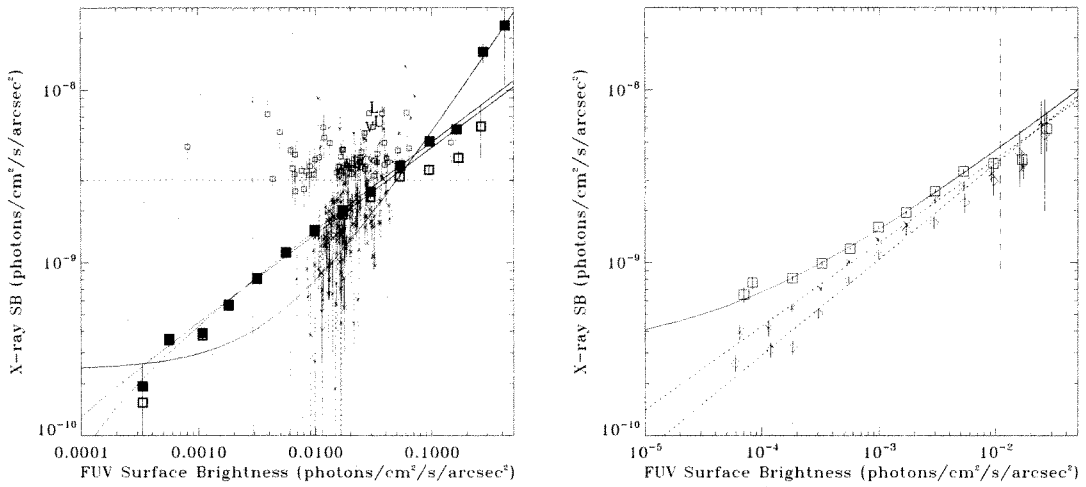

Fig. 17.— **Left:** The X-ray surface brightness as a function of the FUV surface brightness. The large filled □ symbols are the relation for all of the data in the ACIS-S3 mosaic, while the large empty □ symbols are the relation excluding the giant H II regions and the bulge. The small × symbols are for individual FUV knots while the + symbols are for individual X-ray knots. **Right:** The X-ray surface brightness as a function of the FUV surface brightness for the data in the ACIS-S3 mosaic excluding the giant H II regions and the bulge. The □ symbols are for $1'.0 < R < 3'.0$, × symbols for $3'. < R < 4'.0$, and ◇ symbols for $4'. < R < 5'.0$. The smooth lines are functions fitted to data with $FUV < 0.005$ sbu (see text).

TABLE 9
FUV/X-RAY CORRELATION FITS

Radius	A $\times 10^{-10}$ sbu	B $\times 10^{-8}$	β	χ^2_ν	ν
$1'.0<R<3'.0$	$2.93^{+1.18}_{-1.44}$	$4.60^{+1.60}_{-1.16}$	$0.59^{+0.06}_{-0.06}$	2.36	7
$3'.0<R<4'.0$	$-9.20^{+1.34}_{-1.72}$	$3.09^{+1.12}_{-0.80}$	$0.47^{+0.06}_{-0.06}$	2.21	7
$4'.0<R<5'.0$	$-6.18^{+1.06}_{-1.40}$	$3.89^{+2.00}_{-1.42}$	$0.51^{+0.08}_{-0.08}$	2.99	7
		$A \geq 0$			
$1'.0<R<3'.0$	$2.93^{+1.18}_{-1.44}$	$4.60^{1.60}_{-1.16}$	$0.59^{+0.06}_{-0.06}$	2.36	7
$3'.0<R<4'.0$	0	$3.70^{+0.56}_{-0.48}$	$0.49^{+0.02}_{-0.02}$	2.08	8
$4'.0<R<5'.0$	0	$4.83^{+1.28}_{-1.00}$	$0.56^{+0.03}_{-0.03}$	2.71	8
		$A \geq 0$ and $\beta \equiv 0.55$			
$1'.0<R<3'.0$	$3.54^{+0.42}_{-0.42}$	$5.38^{+0.20}_{-0.20}$	0.55	2.47	7
$3'.0<R<4'.0$	$1.12^{+0.40}_{-0.40}$	$5.26^{+0.20}_{-0.20}$	0.55	2.29	8
$4'.0<R<5'.0$	0	$3.22^{+0.08}_{-0.08}$	0.55	3.68	8

tended complexes of star-forming regions, and for the larger complexes we have plotted both the aggregate value and the values for smaller, brighter, sub-regions. The dotted line marks the approximate surface brightness threshold of the X-ray knots.

There are many X-ray regions that lie significantly above the global correlation and those well separated from the main clump are particularly interesting. Some X-ray knots without FUV counterparts might be background clusters. This seems to be the case for the X-ray knot with the lowest FUV surface brightness; there are a large number of background galaxies near this region. Similarly, star-forming regions suffering a large amount of extinction should fall in this region and, indeed, most of the FUV-faint X-ray knots do show evidence of dust lanes. There may also be "fossil" star-forming regions where the X-ray emission persists after the bulk of the massive stellar population has died. Examination of the HST images reveals only three or four regions with X-ray surface brightness above 2.6×10^{-9} sbu and FUV surface brightness below 0.01 sbu which are without a significant population of blue stars and are without ev-

idence of dust lanes or strong absorption. We do not find evidence of "high surface brightness" X-ray emission that is not associated with either H II regions or large populations of young massive stars.

The location of a star cluster on this plot is a complex function of the cluster's mass and age, further complicated by sequential star formation and the uncertainty in the rate at which the X-ray emission fades. Understandably, the two knot selections produce very different results, while the global relation lies between them.

A naïve model: The shape of the FUV/X-ray correlation can be understood in the context of a naïve model of a collection of young star clusters, each composed of a simple stellar population. We assume 1) that the total star formation rate is constant, 2) that every line of sight passes through only a single cluster, 3) that all clusters are characterized by a Kroupa (2001) IMF, 4) that the mass of the cluster is set by the mass of the most massive star formed in the cluster, $m_\star$, using the formulation of Weidner & Kroupa (2006), that every supernova produces the canonical 10^{51} ergs, and 5) the cluster mass function of Weidner et al. (2004). We used the Marigo et al. (2008) isochrones to determine the FUV flux for a grid of stellar masses from 1 to 98 $M_\odot$ and ages from 1 to 200 Myr; and calculated a consistent supernova rate for the same grid. We assumed that every supernova produces the canonical 10^{51} ergs,

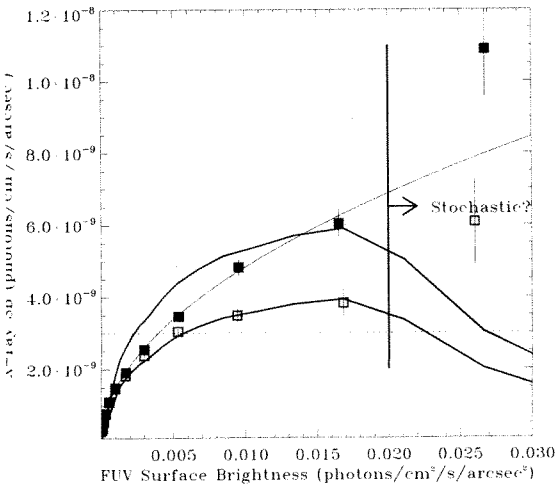

Fig. 18.— The supernova rate as a function of FUV luminosity for a naïve model collection of young stellar clusters. The thick lines are models scaled to the observations. As with the previous figure, empty boxes show the relationship excluding the giant H II regions and filled boxes include all of the data. The thin line is the square root function fitted to the data including the giant H II regions.

but left the efficiency by which the supernova energy is converted to X-rays to be scaled to match the model to the data. The thick solid lines in Figure 18 show the results of this model scaled to match the peak of the model to the L_{FUV} at which the different FUV/X-ray relations diverge strongly. The efficiency was then adjusted to allow the model to fit the data; the required efficiencies are roughly 0.1%. The peak of the model is due to the fact that the clusters with the very highest FUV luminosity have not produced supernovae. The lower cutoff is due to the fact that stars with masses less than 8 $M_\odot$ continue to have FUV emission but do not produce supernovae. The shape of the model relation is similar to that observed when one excludes the giant H II regions. The shape of the relation is not significantly changed by reasonable variation of the input relations.

This model is naïve. It ignores stellar winds, the physical extent of clusters, which may vary with mass and time (cluster dissolution), the uniform FUV emission that is not due to clusters, and the fact that many star-forming regions are not single clusters but are composites. Another naïveté is that while the supernova rate may be instantaneous, the X-ray emission will last much longer than the time step. However, this old X-ray emission may produce no more than a simple offset in the relation, the A parameter in Equation 7. One may further question whether the L_{FUV}/SN rate correlation was extracted from the model in a manner consistent with the way the observed FUV/X correlation was extracted from the data. By selecting all of the image pixels in a given FUV surface brightness interval, one selects the centers of fainter star-forming regions and the peripheries of the brighter star-forming regions, thus combining regions with different $m_\star$; this is equivalent to smoothing the model relation. Despite the shortcomings of this naïve model, it produces roughly the correct shape for the FUV/X-ray correlation.

5.4. Further Morphological Considerations

The Hα emission in M101 is more strongly clumped than the FUV emission due, in part, to stronger scattering of the FUV than of the Hα (Waller et al. 1997). A similar comparison of the FUV and the X-ray might determine whether the X-ray emitting gas is more extended than the FUV emission. Figure 19 (left) shows the FUV and X-ray radial profiles of seventy-five of the brightest individual FUV knots, excluding the Giant H II regions and the bulge. The X-ray and FUV profiles have similar core sizes, but the X-ray profile has broader wings. Since the *GALEX* resolution is 2.″5-3.″0 (HWHM, Martin et al. 2005), while the mean *Chandra* resolution is 2-3″, this is not an effect of the resolution. The broad X-ray wings demonstrate that the average FUV knot is embedded in diffuse X-ray emission, as can be seen by inspection of Figure 3. Whether individual

FUV knots possess an X-ray halo due to hot gas that has expanded beyond the confines of the H II region defined by the FUV emission can not be answered with the current data.

The delay between FUV production and X-ray production, and the long cooling times for X-ray gas suggest that there should be significant X-ray emission downstream of spiral arms, though the X-ray emission need not be immediately downstream of the current sites of vigorous star-formation. Figure 19 (center) is the *GALEX* image of M101 on which has been plotted the flow lines for circular orbits assuming a position angle of 42°, inclination of 21°, and the fit of the rotation curve from Meidt et al. (2009). The length of the flow-lines shows the motion over 10 Myr, a time chosen to produce legible vectors. For most of the region covered by the ACIS-S3 detector, hot gas produced by star-formation in the arm will travel nearly parallel to the arms. Admittedly, this model ignores the deviations in circular orbits due to the gravitational effect of the arms themselves, but such considerations do not change the conclusion that the hottest gas should remain fairly close to the arm, making any X-ray "after-images" from defunct star-forming regions rather difficult to detect.

Despite this difficulty, a simple analysis of the arm profiles is revealing. We can determine whether there is more X-ray emission downstream of FUV knots which, to some extent, define the arms. Using the rotation model described above, we created profiles along the flow direction for each FUV knot (Figure 19 right). The mean FUV profile shows that there is more emission downstream. The notch at $\sim$ 25 Myr is likely due to the low probability of two star-forming regions forming close together along the same flow-line. The X-ray emission mimics the FUV emission but is far stronger, suggesting contributions from older star-forming regions that are no longer FUV bright. However, confusion by close successive spiral arm segments along the flow lines mean that such an analysis can not place any meaningful constraint on the X-ray cooling times for this galaxy.

5.5. Spectroscopy

Comparison with our previous results: The spectroscopic analysis here is much finer than that of KMSP; this improvement is not due solely to the larger number of counts and more uniform coverage of the brightest portion of the disk. The stowed data produce much higher signal-to-noise particle background spectra, and the data are dependable to 0.35 keV, while KMSP limited their study to above 0.45 keV. Use of the ACIS-S1 data for background analysis was not possible for KMSP, but now yields a dependable measure of the Galactic foreground spectrum that is uncontaminated by the emission from M101.

Caveats on the meaning of spectral fits: As noted above, it is generally not possible to determine from these spectra whether the emitting plasmas are in CIE or not, particularly since, at any spatial resolution, the spectrum will be the product of multiple emission components. Except in some extreme cases, the CIE models represent the spectral shape of NEI spectra reasonably well, even if they do not provide good measures for the true electron temperatures. Further, given that multiple components contribute to the spectrum any division between CIE and NEI components is not likely to be unique.

The best fit required three CIE components with $kT = (0.112, 0.279, 0.812)$ keV, followed by a fit with two CIE components with $kT = (0.113, 0.292)$ keV, whereas fits restricted to $E > 0.45$ keV are well fit with $kT = (0.192, 0.601)$ keV. Fitting the giant H II regions for $E > 0.35$ keV produced kT = (0.2-0.25,0.6-0.7) keV. This spread of temperatures among the different fits suggests a continuous distribution of emission measure, but a simple power law distribution did not fit the data any better. Since the global spectrum is summed over many different emitting regions, one might expect a variety of temperatures and thus a "lumpy" distribution of emission measure.

To determine the extent to which the spectrum is described by a discrete rather than continuous distribution we performed the following exercise. We assumed a three CIE component model. For each temperature in $0.08 < kT < 1.0$, in steps of $kT = 0.02$, and each normalization in $-7.0 < \log_{10} N < -5.0$, in steps of $\log_{10} N = 0.1$, we determined the best fit after fixing one component at that (kT_f, N_f) and allowing the other two components to vary. There are multiple ways of analysing the results of this "sweep" search. For a given lT_f, one can consider the best fit or the fit with the greatest N_f producing a χ^2 smaller than some value. In neither case is the result trivial to interpret; given a spectrum produced by two CIE components at kT_S and kT_H, introducing a component kT_f such that $kT_S < kT_f < kT_H$ will cause the fitted kT_S to be less than the true kT_S, the fitted kT_H to be greater than the true kT_H, and both fitted normalizations to be lower than their true values.

Figure 20 (Left) plots the fit parameters for all three components for the best fit to the global spectrum at a given kT_f. The emission measure has a peak at $\sim$ 0.1 keV, a peak at 0.25-0.3 keV, and a much broader peak at $\sim$ 0.6 keV, consonant with the two and three CIE component fits. Simulations of power law DEM spectra with equivalent exposure, FOV, and response produce a smooth distribution of components following the the power law in the kT_f,N_f plot rather than this multiply peaked distribution. Simulations of the three CIE component model yielded a similarly broad distribution of fitted temperatures for the highest temperature component, suggesting that the temperature cannot be well

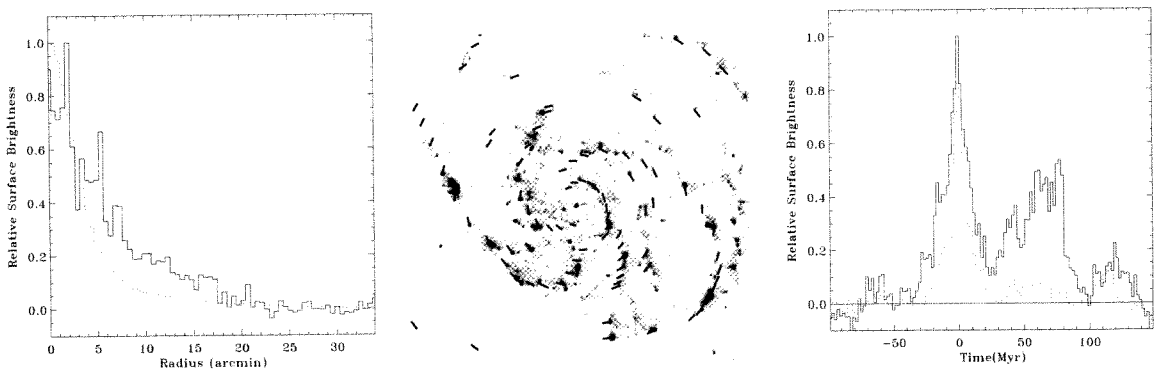

Fig. 19.— The *GALEX* image of M101 with the flow-lines marked for several of the strongly X-ray emitting arms, as well as a number of other FUV knots. The length of each vector is the distance traveled on a circular orbit in 10 Myr.

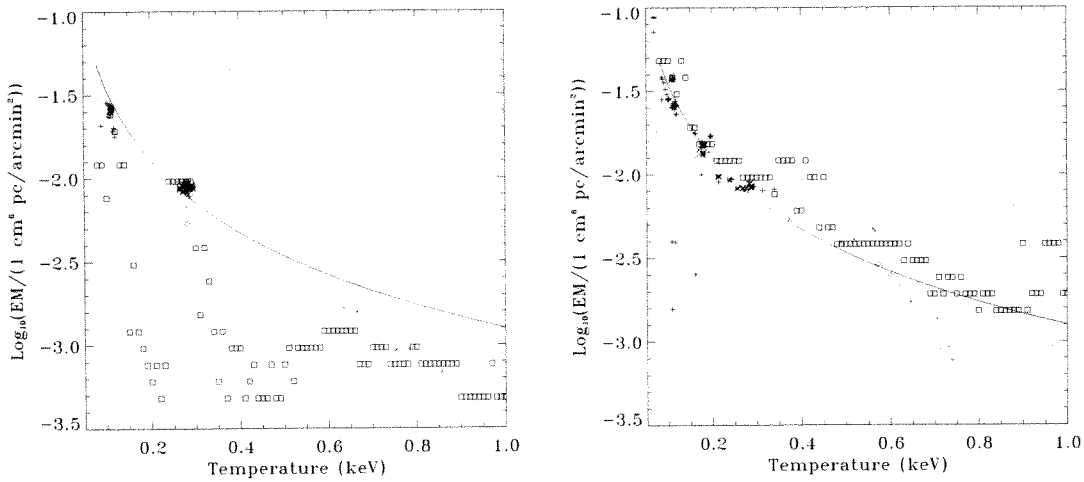

Fig. 20.— The results of a three CIE component sweep search fit where one component was fixed in temperature and normalization, kT_f, N_f, while the other two were adjusted to minimize χ^2. The boxes are the parameters of the fixed component, the + are the parameters of the softer of the two floating components, and the × are the parameters of the harder of the two floating components. **Left:** Plot of results for the best χ^2 for each kT_f. **Right:** Plot of results for the greatest value of N_f producing a $\chi^2 < 1.5$ for each value of kT_f. The solid line in both plots is a power law with $\alpha = -1.44$ and an arbitrary normalization.

constrained by the data of this quality or resolution; the width need not be intrinsic but may be so.

Figure 20 (Right) plots the fit parameters for all three components for the highest normalization N_f possible at each kT_f while keeping $\chi^2 < 1.5$. The solid line is a power law with the index from the DEM fit and an arbitrary normalization; it follows the kT-N relationship very well, with the exception of the region around 0.25-0.3 keV, where there is a strong peak in the left panel. Thus it would seem that the index of the power law DEM fit is set by the χ^2 envelope but the true distribution of emission measure is more complicated than a power law, and is more similar to the multi-component fit.

This analysis can be extended one step further to consider the effects of fitting a power law DEM with two or three CIE components. Figure 21 shows the temperatures of two component fits to a power law DEM of index α, minimum temperature cutoff of 0.08 keV, and a maximum temperature cutoff of kT_c. For $-1.5 < \alpha < 1.5$, the two components have temperatures of ~ 0.2 keV and ~ 0.6 keV, and the temperatures increase only slightly with α. The temperature of the hotter component increases more rapidly with the upper cutoff temperature. Three component fits for $\alpha < -1$ produce component temperatures of ~ 0.1 keV, $0.2 - 0.25$ keV, and $0.45 - 0.6$ keV. At higher α the fits tend to two component solutions. The details

are relatively unimportant; the lesson is that at CCD resolution, nearly any continuous distribution of emission measure, when fit by two CIE components, produces nearly the same fit temperatures, even though the spectra have very different shapes.

Thus, for the high quality spectra of M101, the fitted temperatures appear to represent the underlying distribution. For lower quality spectra, the fitted temperatures, particularly those around $kT = (0.2, 0.6)$ keV are highly suspect as many different distributions can produce the same fitted temperatures.

In M101, the soft excess drives the fit; excluding $E < 0.45$ allows the typical $kT = (0.2, 0.6)$ keV fit, while including that spectral range requires a third component at ~ 0.1 keV, which then pushes the other components to higher temperatures. As discussed in §4.5, this soft component is real, and our preliminary analysis of *Chandra* data of M83, the only other galaxy with sufficient quality data in $0.35 < E < 0.45$ suggests a similar soft excess. Owen & Warwick (2009) note a similar excess in the *XMM-Newton* spectra of the diffuse emission in M51 and M83 and suggest that it is due to a power-law component with $\Gamma \sim 2.9$. Such a component is not compatible with our data unless strongly absorbed below 0.4 keV.

The spectrum is thus described by a soft component at ~ 0.1 keV, a narrow distribution of temperatures around 0.25 keV, and a broad distribution of temperatures around 0.6 keV. Although the broad distribution around 0.6 keV is due, in part, to uncertainty in the fits, we cannot rule out an intrinsically broader distribution of temperatures.

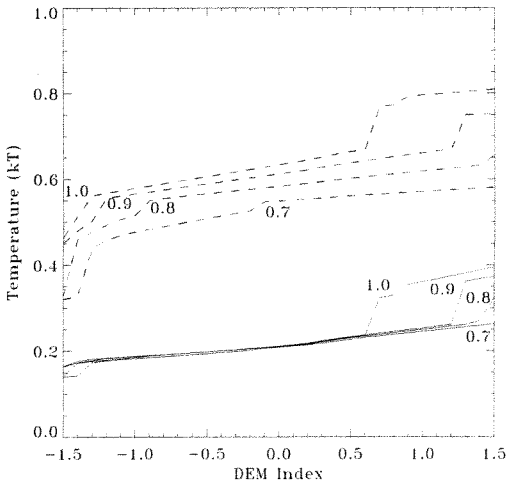

Fig. 21.— The component temperatures derived by fitting a powerlaw DEM spectrum with index α and the high temperature cutoff listed, with a two CIE component model. Each curve is labeled with the high temperature cutoff, kT_c, in keV.

Comparison with other galaxies: A number of late-type galaxies have been fit with two thermal models and have been found to have temperatures of 0.2-0.25 and 0.6-0.75; NGC 224 (Trudolyubov et al. 2005), NGC 2403 (Fraternali et al. 2002), NGC 4303 (Jiménez-Bailón et al. 2003), NGC 6946 (Schlegel et al. 2003), and a round half-dozen by Owen & Warwick (2009). There are a few that do not fit this mold, such as NGC 3184 (Doane et al. 2004). There are a wide variety of techniques for handling the backgrounds, abundances, and internal absorption, as well as differences in the fitted energy ranges, which can lead to a large variation in the fitted temperatures. Despite the large variety of analysis techniques, the bulk of these disks can be characterized by $kT \sim 0.2$-0.25 and $kT \sim 0.6$-0.75, the typical temperatures obtained from most DEM distributions with reasonable cut-off temperatures. Thus the temperatures are not the parameter of interest for comparing the emission from different galaxies, it is the ratio of the emission measures of the components, which is a quantity not so frequently listed. These temperatures are alos similar to those of Galactic star-forming regions, which are subject to the same fitting uncertainties.

Comparison to the Galaxy: The temperatures determined for the global spectrum of M101 are similar to temperatures of Galactic emission. Many large features have temperatures of ~ 0.25 such as the Galactic halo (Kuntz & Snowden 2000) and the Loop I superbubble (Willingale et al. 2003). The line of sight towards $(\ell, b) = (111°, 1°)$ studied by Kuntz & Snowden (2008) showed local (D<3 kpc) 0.25 keV emission, and 0.6 keV emission on the far side of the Perseus arm, perhaps due to star formation there. The average ~ 0.250 Galactic halo component towards the North Galactic Pole (which does not include the bulk of the local disk emission) has an emission measure of 8.8×10^{-4} cm^{-6} pc (Kuntz et al. 2001), which is equivalent to a surface brightness of 1.6×10^{-11} sbu in M101. This is slightly less than the surface brightness in the dark interarm region between NGC 5462 and the bulk of the disk. If the halo of M101 is similar to that of the Galaxy, it is overwhelmed by the disk emission.

Comparison to Galactic Star-Forming regions: The most apt comparison to M101 would be star-forming regions in the Galaxy or Magellanic Clouds. Those star-forming regions sufficiently unabsorbed to allow meaningful spectral fits down to 0.35 keV are typically sufficiently large that they have been observed only with the ACIS-I, whose response at O VII is poor. However, the observations of the Rosetta nebula ($kT = 0.06, 0.8$ keV), and the Omega nebula ($kT = 0.13, 0.6$ keV) (both Townsley et al. 2003) show a similar two component structure. Several other nebula with strong absorption show a range of single component temper-

atures; 30 Doradus (kT = 0.58 keV Townsley et al. 2006), NGC 6357 (kT = 0.6 keV Wang et al. 2007), the Lagoon nebula (kT = 0.63 keV Rauw et al. 2002), and Cepheus B (kT = 0.8 keV Getman et al. 2006). Although the spread of temperatures from the single temperature fits might compensate for softer components, the two component fits suggest a real variation in the temperature of the harder component. The ratio of the emission measures, where fit, have not been published, so that comparison is impossible.

On the hardness ratio/surface brightness relation. The hardness ratio increases with the X-ray surface brightness and the X-ray surface brightness increases with the UV surface brightness, and thus the star-formation rate. One should be able to observe the same relation in other galaxies to determine the extent of the effect of metallicity, disk surface density, and other local effects. Since, at least in late-type disks such as M101, the emission due to star-formation dominates, the global hardness ratio should reflect the global star-formation rate to the extent that local effects do not matter. As one moves to earlier type disks, this relation should fail as the stellar emission begins to dominate. However, a better characterization of the spectrum of the stellar emission might allow one to untangle the various effects, again using the K-band emission as a tracer of the stellar mass.

6. Summary

Because M101 is face-on, there is no clear way to separate the halo/thick disk emission from the thin disk/star-formation component. Comparison to the Galaxy suggests that the halo emission in M101 is overwhelmed by the disk emission. The change in the FUV/X-ray correlation with radius suggests that no more than 20% of the emission in the center can be due to the sum of the halo, the stellar emission, and emission due to star formation older than that traced by the brihgt FUV emission. Even less emission is available for these components at larger radii. Thus, not separating the halo from the disk does not pose a significant problem for the analysis of the diffuse emission.

The bulk of the X-ray emission is due to current and recent star-formation. Residual X-ray binaries account for 4% of the unresolved flux, while unresolved stars account for $\lesssim$ 3% of the diffuse flux. A large contribution from stars would produce a radial change in the X-ray hardness ratio that is not observed.

One would expect the bulk of the emission due to star-formation to be produced by supernovae. However, the contribution of individual supernova remnants is relatively low; the bulk of the emission must originate with remnants that have lost their identity as individual remnants. The relation between the X-ray and FUV surface brightness is non-linear, as one might expect from the continuous formation and evolution of stellar clusters that lose FUV emission rapidly as the X-ray emission increases. Similarly, one should not expect, and does not see, a strict knot-to-knot correlation between the X-ray and FUV; several of the star-forming regions are probably too young to produce significant X-ray emission, while there are a few X-ray knots without FUV emission that may be fossil star-forming regions. We find that, in a statistical sense, the emission downstream of spiral arms has a higher X-ray/FUV ratio, as expected from an aging stellar population. However, due to confusion, one cannot place limits on the cooling time of the X-ray emitting gas.

The hardness ratios from the imaging analysis and the spectral fits show that, on average, the X-ray emission becomes harder as the surface brightness increases. However this relation does not allow one to separate X-ray emission from current star formation from that due to less recent star formation.

The global spectrum is complex and not well fit. It appears to be composed of a soft component with $kT \sim 0.1$ keV, a second component with a distribution of temperatures between 0.2 and 0.3 keV, and a third component with a, possibly intrinsically, broad distribution of temperatures centered on $\sim$ 0.6 keV. Fits allowing the abundance of the iron-group elements to vary produced reasonable values for the iron abundance and produced two component fits of equivalent quality. In general, at CCD spectral resolution, although the formal errors are small, it appears that the temperatures are poorly determined, with many different temperature distributions producing the same fitted temperatures. As a result, comparing temperatures between galaxies is not nearly as informative as comparing the ratios of the emission measures of those components.

We would like to thank Jurgen Kamphuis for providing the H I data, and Benne Holwerda for facilitating the transfer. We would like to thank Tamara Helfer for use of the ^{12}CO data. We would like to thank Keith Arnaud, Luciana Bianchi, Leigh Jenkins, Knox Long, Gerhard Meurer, Richard Mushotzky, David Strickland, and Stuart Vogel for many useful discussions over the very long gestation of this work. KDK would also like to thank the late David Reuben Ramirez for some interesting discussions early in this project.

KDK was funded by Chandra grant XXX.

This research has made use of data obtained from the Chandra X-ray Observatory, the Chandra Data Archive, and the CIAO software package provided by the Chandra X-ray Center (CXC) This paper was based in part on observations obtained with XMM-Newton, an ESA science mission with instruments and contributions directly funded by ESA Member States and NASA. This research has made use of the NASA/IPAC Infrared Science Archive, which is operated by the Jet

Propulsion Laboratory, California Institute of Technology, under contract with the National Aeronautics and Space Administration. Some of the data presented in this paper were obtained from the Multimission Archive at the Space Telescope Science Institute (MAST). STScI is operated by the Association of Universities for Research in Astronomy, Inc., under NASA contract NAS5-26555. Support for MAST for non-HST data is provided by the NASA Office of Space Science via grant NAG5-7584 and by other grants and contracts.

A. Soft Proton Contamination

Since X-ray photons, unlike fruits in the market, are not marked by their mechanism of origin, when the emission of interest fills the entire field of view (as in studies of diffuse Galactic emission) one can separate emission components only by their spectral shape. Thus one must have as many independent characterizations of the various back/foreground components as possible. Long duration flares with only low-amplitude variation can easily be missed, while low-amplitude flares with durations on the order of a kilosecond can be very difficult to remove. Thus the emission due to the soft proton flares can be significant even after light-curve cleaning; in the 0.45-1.0 keV band they can produce as much as a tenth of the flux of the Galactic foreground.

Although the backside-illuminated chips (ACIS-S1 and ACIS-S3) are far more sensitive to the soft proton flares, the bulk of the published discussion of the spectral shape of this emission has concerned the front-side illuminated chips (Hickox & Markevitch 2006). A short discussion of the ACIS-S3 can be found in Markevitch et al. (2003), where they noted that the spectral shape of several flares affecting their data could be fitted by a power law with an exponential cutoff where the photon index of the power law was -0.1 and the cutoff energy ranged from ~ 5 to 7 keV. The fitting was done with the redistribution matrix but without the effective area function. All of the observed flares had a similar spectral shape.

In order to fit the background spectra for M101, we needed a reasonable characterization of the spectrum of the residual soft proton emission for both the ACIS-S3 and ACIS-S1 chips. We attempted this characterization using flared observations that had been acquired for a number of different studies. The observations used are listed in Table 10.

For each obsid we cleaned the light-curve using a method similar to that described in Kuntz & Snowden (2008), removing periods when the 2.0-7.0 keV count rate was more than 3σ above the mean. We then extracted a spectrum over the entire chip from the uncleaned event file, and another from the same area from the cleaned event file. We then scaled both spectra by their exposure times, and subtracted the clean spectrum from the uncleaned spectrum. We then fitted that result using a unit diagonal response.

We used a functional form similar to that used by Markevitch et al. (2003)

$$NE^{-\Gamma} \begin{cases} \exp\left(\frac{E_c - E}{E_b}\right) \\ 1 \end{cases} \qquad \text{(A1)}$$

and found that it fit all of the flares reasonably well. This functional form has the advantage that many of the parameters could be fixed for all of the flare spectra; fixing the photon index Γ to 0.0 increased χ^2 by $\sim 4\%$, and fixing the cut-off energy E_c to 0.0 changed χ^2 by even an smaller amount. Only for the spectra with the highest numbers of counts (> 50000 counts in 0.35-13.0 keV) were the differences between fixed and floating parameter fits visible by inspection. The "fixed parameter" fits for ACIS-S3 are shown in the left-hand panel of Figure 22. The remaining parameters, which were allowed to vary, are the e-folding energy (E_b) and the normalization (N). For ACIS-S3, these two quantities are not correlated though there may be some complicated relation between the two. We find that the observations studied by Markevitch et al. (2003) form a more uniform sample than our expanded sample and that given only that limited sample we would have reached conclusions similar to those of Markevitch et al. (2003).

The situation is somewhat different for ACIS-S1. First, the ACIS-S1 soft proton count rate is much lower than that in ACIS-S3, perhaps as a result of vignetting. Further, the ACIS-S1 soft proton count rate is not correlated with the ACIS-S3 soft proton count rate. The ACIS-S1 flare spectra shown in Figure 22 are very flat, with very little sign of a cut-off. We find the ACIS-S1 count rate (or normalization) to be correlated with the e-folding energy of the ACIS-S3 spectra in the sense that the flatter the ACIS-S3 spectrum, the stronger the spectrum in ACIS-S1. For many of the ACIS-S1 spectra, the total number of counts is quite low, however, the strongly smoothed spectra shown in the right-hand panel of Figure 22 show that the spectra are usually quite flat. Consequently, fitting the exponential cut-off with a variable e-folding energy and fitting with a pure power law produced the same values of χ^2 despite the very different shapes of those two functions. For the lowest flare levels, the fits to ACIS-S1 were very close to flat.

It should be noted that the flares studied here are stronger than the typical flares not removed by light-curve cleaning. We cannot test our functional form directly on these very low amplitude flares. However, our functional form is sufficiently flexible to fit the variety of flare spectral shapes seen at higher levels; the low-amplitude flares would have to have a very different spectral shape not to be reasonably well handled by our functional form. Thus we recommend fitting the ACIS-S3 soft proton emission by

$$N \exp\left(\frac{-E}{E_b}\right) \qquad \text{(A2)}$$

where the e-folding energy E_b is typically 3-10 keV, but can be much larger for the flattest spectra. The ACIS-S1 soft proton emission *can* be fit with the same function, but usually a power law with a photon index of 0.0 is sufficient.

A more systematic plundering of the archive for long exposures with significant (but not overly large) flaring could improve this analysis substantially.

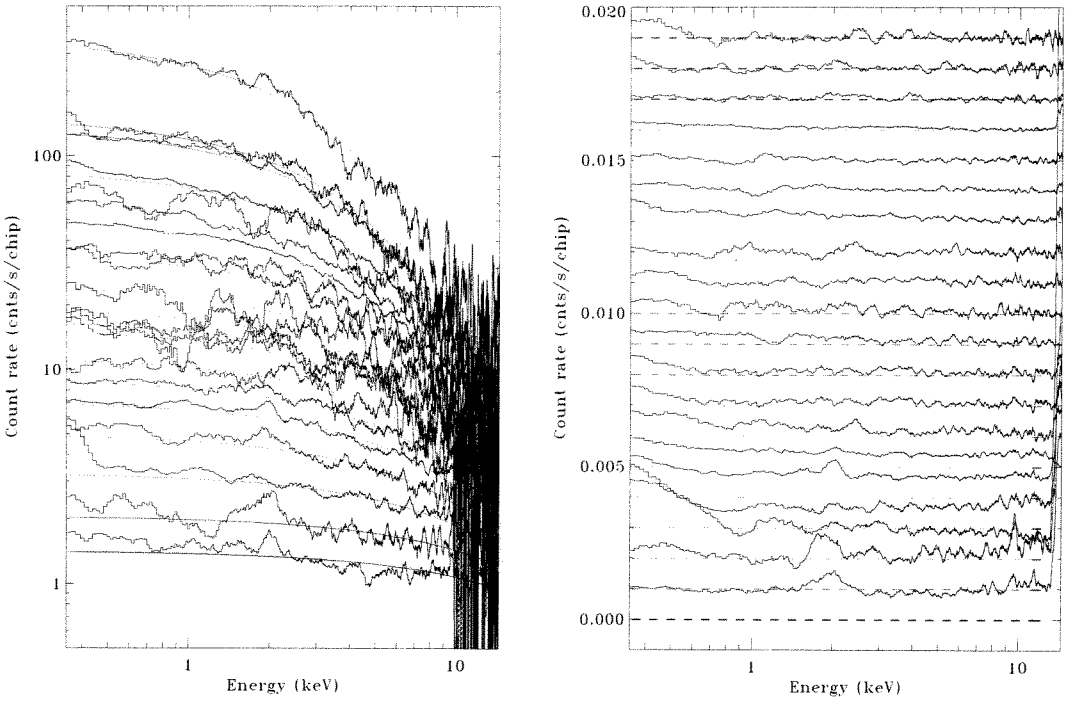

Fig. 22.— **Left:** The difference spectra for ACIS-S3 smoothed by a 277 eV (19 PI bin) wide boxcar function. The spectra were all normalized at 10.0 keV, then successively shifted upwards for clarity. The scaling axes are both logarythmic. The order of the spectra is given in Table 10, with 19 at the top and 1 at the bottom. **Right:** The difference spectra for ACIS-S1. The vertical scale is linear. The dashed lines show the zero-level for each spectra; note that spectra often overlap towards the bottom of the plot. The order of the spectra is the same as in the previous panel.

TABLE 10
SOFT PROTON DATA

Obsid	Total Exposure (ks)	Clean Exposure (ks)	ACIS-S3 Counts[a]	ACIS-S1 Counts	Index Number[b]
326	42.1	36.8	14652	120	17
650	95.3	66.9	46804	1321	16
766	38.5	26.7	72793	1215	13
793	50.9	48.9	5683	53	19
930	38.1	25.1	24724	604	14
1520	23.7	19.3	4198	81	18
1934	29.3	24.7	5571	371	8
1969	26.7	23.0	7553	137	11
2030	26.4	19.1	4346	152	15
2149	28.0	24.2	7048	574	7
2206	18.7	14.9	6870	44	12
2213	58.3	55.6	4054	184	10
3932	47.9	43.3	5223	505	9
3951	89.0	75.9	24357	5012	6
4733	24.3	6.3	33603	16238	1
4743	27.2	23.0	8913	4689	2
5297	21.6	14.3	18510	4958	4
6114	65.8	48.0	55205	11137	5
6152	33.8	26.7	45781	5738	3

[a]The number of counts in the difference spectrum for ACIS-S3.

[b]The order of the spectrum in Figure 22; the lower the index, the lower the ACIS-S3 normalization.

REFERENCES

Boissier, S., et al. 2007, ApJS, 173, 524

Bresolin, F. 2007, ApJ, 656, 186

Chen, L.-W., Fabian, A. C., & Gendreau, K. C. 1997, MNRAS, 285, 449

Chiappini, C., Romano, D., & Matteucci, F. 2003, MNRAS, 339, 63

De Luca, A., & Molendi, S. 2004, A&A, 419, 837

de Vaucouleurs, G., de Vaucouleurs, A., Corwin, H. G., Buta, R. J., Paturel, G., & Fouque, P. 1991, Third Reference Catalogue of Bright Galaxies (Springer-Verlag)

Doane, N. E., Sanders, W. T., Wilcots, E. M., & Juda, M. 2004, AJ, 128, 2712

Fabbiano, G., & Shapley, A. 2002, ApJ, 565, 908

Franciosini, E., Pallavicini, R., & Sanz-Forcada, J. 2005, A&A, 446, 501

Fraternali, F., Cappi, M., Sancisi, R., & Oosterloo, T. 2002, ApJ, 578, 109

Getman, K. V., Feigelson, E. D., Townsley, L., Broos, P., Garmire, G., & Tsujimoto, M. 2006, ApJ, 163, 306

Helfer, T. T., Thornly, M. D., Regan, M. W., Wong, T., Sheth, K., Vogel, S. N., Blitz, L., & Bock, D. C.-J. 2003, ApJS, 145, 259

Hickox, R. C., & Markevitch, M. 2006, ApJ, 645, 95

Jarrett, T. H., Chester, T., Cutri, R., Schneider, S., & Huchra, J. P. 2003, AJ, 125, 525

Jiménez-Bailón, E., Santos-Lleó, J. M., Mas-Hesse, J. M., Guainazzi, M., Colina, L., no, M. C., & Delgado, R. M. G. 2003, ApJ, 593, 127

Kamphuis, J. 1993, Ph.D. thesis, Rijksuniversiteit Groningen

Kamphuis, J., Sancisi, R., & van der Hulst, T. 1991, A&A, 244, L29

Kennicutt, R. C., Bresolin, F., & Garnett, D. R. 2003, ApJ, 591, 801

Kroupa, P. 2001, MNRAS, 322, 231

Kuntz, K. D., & Snowden, S. L. 2000, ApJ, 543, 195

Kuntz, K. D., & Snowden, S. L. 2001, ApJ, 554, 684

Kuntz, K. D., & Snowden, S. L. 2008, A&A, 478, 575

Kuntz, K. D., Snowden, S. L., & Mushotzky, R. F. 2001, ApJ, 548, L119

Kuntz, K. D., Snowden, S. L., Pence, W., & Mukai, K. 2003, ApJ, 588, 264

Long, K. S., et al. 2009, ApJ

Marigo, P., Girardi, L., Bressan, A., Groenewegen, M. A. T., Silva, L., & Granato, G. L. 2008, A&A, 482, 883

Markevitch, M., et al. 2003, ApJ, 583, 70

Marshall, H. L., Tennant, A., Grant, C. E., Hitchcock, A. P., O'Dell, S., & Plucinsky, P. P. 2004, Proceedings of SPIE, 5165, 497

Martin, D. C., et al. 2005, ApJ, 619, L1

Matonick, D. M., & Fesen, R. A. 1997, ApJS, 112, 49

Meidt, S. E., Rand, R. J., & Merrifield, M. R. 2009, ApJ, 702, 277

Moretti, A., Campana, S., Lazzati, D., & Tagliaferri, G. 2003, ApJ, 588, 696

Owen, R. A., & Warwick, R. S. 2009, MNRAS, 394, 1741

Rauw, G., Nazé, Y., Gosset, E., Stevens, I. R., Blomme, R., Corcoran, M. F., Pittard, J. M., & Runacres, M. C. 2002, A&A, 395, 499

Revnivtsev, M., Churazov, E., Sazanov, S., Forman, W., & Jones, C. 2007, A&A, 473, 783

Saha, A., Thim, F., Tammann, G. A., Reindl, B., & Sandage, A. 2006, ApJS, 165, 108

Sandage, A., & Bedke, J. 1994, The Carnegie Atlas of Galaxies (Carnegie Insitute of Washington)

Schlegel, E. M., Holt, S. S., & Petre, R. 2003, ApJ, 598, 982

Snowden, S. L., et al. 1997, ApJ, 485, 125

Snowden, S. L., & Kuntz, K. D. 1998, Cookbook for analysis procdures for *rosat* xrt observations of extended objects and the diffuse background, part i: Individual observations, Technical report, NASA/GSFC

Snowden, S. L., & Kuntz, K. D. 2008, A&A, 478, 615

Snowden, S. L., & Pietsch, W. 1995, ApJ, 452, 627

Thilker, D. A., et al. 2007, ApJS, 173, 572

Townsley, L. K., Broos, P. S., Feigelson, E. D., Brandt, B. R., Chu, Y.-H., Garmire, G. P., & Pavlov, G. G. 2006, ApJ, 131, 2140

Townsley, L. K., Feigelson, E. D., Montmerle, T., Broos, P. S., Chu, Y.-H., & Garmire, G. P. 2003, ApJ, 593, 874

Trudolyubov, S., Kotov, O., Priedhorsky, W., Cordova, F., & Mason, K. 2005, ApJ, 634, 314

Tyler, K., Quillen, A. C., LaPage, A., & Rieke, G. H. 2004, ApJ, 610, 213

Vázquez, G. A., & Leitherer, C. 2005, ApJ, 621, 695

Waller, W. H., et al. 1997, ApJ, 481, 169

Wang, J., Townsley, L. K., Feigelson, E. D., Getman, K. V., Broos, P. S., Garmire, G. P., & Tsujimoto, M. 2007, ApJS, 168, 100

Warwick, R. S., Jenkins, L. P., Read, A. M., Roberts, T. P., & Owen, R. A. 2007, MNRAS, 376, 1611

Weidner, C., & Kroupa, P. 2006, ApJ, 365, 1333

Weidner, C., Kroupa, P., & Larsen, S. S. 2004, MNRAS, 350, 1503

Willingale, R., Hands, A. D. P., Warwick, R. S., Snowden, S. L., & Burrows, D. N. 2003, MNRAS, 343, 995

Wilms, J., Allen, A., & McCray, R. 2000, ApJ, 542, 914

This 2-column preprint was prepared with the AAS LaTeX macros v5.0.